Journal of Sound and Vibration 333 (2014) 283–306

Contents lists available at ScienceDirect

Journal of Sound and Vibration

journal homepage: www.elsevier.com/locate/jsvi

On vortex–airfoil interaction noise including span-end effects, with application to open-rotor aeroacoustics

Michel Roger [a,*], Christophe Schram [b], Stéphane Moreau [c]

[a] Laboratoire de Mécanique des Fluides et Acoustique, École Centrale de Lyon, 69134 Écully, France
[b] Von Kármán Institute, 1640 Rhode St-Genèse, Belgium
[c] Département de Génie Mécanique, Université de Sherbrooke, Québec, Canada J1K2K1

ARTICLE INFO

Article history:
Received 19 March 2013
Received in revised form
6 September 2013
Accepted 10 September 2013
Handling Editor: R.E. Musafir
Available online 10 October 2013

ABSTRACT

A linear analytical model is developed for the chopping of a cylindrical vortex by a flat-plate airfoil, with or without a span-end effect. The major interest is the contribution of the tip–vortex produced by an upstream rotating blade in the rotor–rotor interaction noise mechanism of counter-rotating open rotors. Therefore the interaction is primarily addressed in an annular strip of limited spanwise extent bounding the impinged blade segment, and the unwrapped strip is described in Cartesian coordinates. The study also addresses the interaction of a propeller wake with a downstream wing or empennage. Cylindrical vortices are considered, for which the velocity field is expanded in two-dimensional gusts in the reference frame of the airfoil. For each gust the response of the airfoil is derived, first ignoring the effect of the span end, assimilating the airfoil to a rigid flat plate, with or without sweep. The corresponding unsteady lift acts as a distribution of acoustic dipoles, and the radiated sound is obtained from a radiation integral over the actual extent of the airfoil. In the case of tip–vortex interaction noise in CRORs the acoustic signature is determined for vortex trajectories passing beyond, exactly at and below the tip radius of the impinged blade segment, in a reference frame attached to the segment. In a second step the same problem is readdressed accounting for the effect of span end on the aerodynamic response of a blade tip. This is achieved through a composite two-directional Schwarzschild's technique. The modifications of the distributed unsteady lift and of the radiated sound are discussed. The chained source and radiation models provide physical insight into the mechanism of vortex chopping by a blade tip in free field. They allow assessing the acoustic benefit of clipping the rear rotor in a counter-rotating open-rotor architecture.

1. Introduction

This paper presents an analytical investigation on the impingement of a cylindrical vortex on a thin rigid airfoil and the associated sound radiation. The vortex axis is assumed in a plane perpendicular to the airfoil plane. This generic vortex–airfoil interaction mimics a class of mechanisms encountered in rotating blade technology, for which the associated acoustic signature is a crucial concern. In particular the main motivation of the work is the understanding of blade–tip effects in the rotor–rotor interaction tonal noise generated by advanced counter-rotating open rotors (CRORs). CRORs are identified as an

* Corresponding author. Tel.: +33 4 72 18 60 11; fax: +33 4 72 18 91 43.
E-mail address: michel.roger@ec-lyon.fr (M. Roger).

0022-460X/$ - see front matter © 2013 Elsevier Ltd. All rights reserved.
http://dx.doi.org/10.1016/j.jsv.2013.09.012

Nomenclature

A_0	amplitude factor of the exponential vortex
a, a_1, a_2, b	combined non-dimensional wavenumbers
c	airfoil chord
c_0	speed of sound
e	blade–tip to vortex–radius distance
E, E^*	Fresnel integrals
$\tilde{G}$	two-dimensional wavenumber spectrum
$\mathcal{I} = \mathcal{I}_1 + \mathcal{I}_2$	chordwise radiation integrals
K	total non-dimensional aerodynamic wavenumber
$k = \omega / c_0$	acoustic wavenumber
(k_1, k_2)	chordwise and spanwise aerodynamic wavenumbers
(k_1', k_2')	same as (k_1, k_2) with sweep
$L = 2d$	span length
$\ell = \ell_1 + \ell_2$	unsteady lift on a blade segment
$M_{0,1,2} = U_{0,1,2}/c_0$	Mach numbers
p	acoustic pressure
(r, θ)	cylindrical coordinates around vortex axis
r_0	vortex core radius
R_0	radius of rotor annulus
S_0	convection-corrected distance
T	relative rotor–rotor interaction period
U_0	incident flow speed
U_c	chordwise convection speed
$V = \Omega R_0$	tangential speed
w	upwash velocity (normal to a blade surface)
w_0	gust amplitude
(x_1, x_2, x_3)	observer Cartesian coordinates
(y_1, y_2, y_3)	source Cartesian coordinates without sweep
(y_1', y_2', y_3)	source Cartesian coordinates with sweep
(X, Y)	axial and tangential coordinates
α	skewness angle of a gust
γ	stagger angle of a blade
Γ	vortex strength
$\beta = \sqrt{1 - M_0^2}$	compressibility parameter
$\beta_{1,2} = \sqrt{1 - M_{1,2}^2}$	partial compressibility parameter
κ, κ'	supercritical and sub-critical Helmholtz parameters
λ	acoustic wavelength
ϕ, ϕ', Φ	velocity disturbance potentials
φ	vortex inclination angle
$\Phi^{(0)}$	complex error function with complex arguments
ψ	sweep angle
ρ_0	mean fluid density
ω	angular frequency
Ω	fan rotating speed

Subscripts/superscripts

$(\cdot)^*$	made non-dimensional by $c/2$, or complex conjugate
$\tilde{(\cdot)}, \hat{(\cdot)}$	Fourier transforms
$(\cdot)_0$	incident-flow related quantity
$(\cdot)_1$	chordwise quantity
$(\cdot)_2$	spanwise quantity

alternative to the turbofan-engine technology for future aircraft propulsion. They are characterized by lower fuel consumption and higher propulsive efficiency associated with equivalent very high by-pass ratios, up to 25 or 30. But the main concern is about the noise exposure around airports during take-off and landing because the blades operate in free field. Furthermore even if a CROR system is mounted at the rear of a fuselage in order to minimize cabin noise, the comfort of passengers remains another challenging issue. This is why efforts are presently made in the aeroacoustic community towards acoustic prediction strategies that can be used at the early design stage, in order to define low-noise configurations with the help of optimization algorithms.

The most annoying acoustic signature of CRORs at low and moderate frequencies is tonal noise associated with all periodic aerodynamic fluctuations experienced by the rotating blades. This includes various mechanisms. Typically the mounting on the airplane is responsible for stationary inflow distortions due to the vicinity of the fuselage, the flow deviation associated with the mean lift of the wing and the wake of the pylon. This contribution is not intrinsic to the technology but is rather qualified as an installation effect. It radiates at harmonics of the blade passing frequencies of both rotors and involves both rotors nearly independently. Other sources are intrinsic to the counter-rotating propulsive system in the sense that they do not essentially depend on the installation. Firstly, the wakes shed from the front rotor impinge on the blades of the rear rotor and produce what is called wake–interaction noise. Secondly, the potential field of the rear rotor can induce lift fluctuations on the blades of the front rotor, generating potential-interaction noise. Finally, the tip vortices shed from the front rotor can also be chopped by the rear rotor depending on the compared tip radii and/or operational conditions. Both wake impingement and blade/tip–vortex interactions involve sources distributed on the rear-rotor blades, whereas potential-interaction noise is radiated from the front rotor. All these interactions radiate at linear combinations of multiples of the blade passing frequencies of both rotors, for this reason the acoustic signature is referred to as combination tones. The present focus is on the fundamental aspects of blade/tip–vortex interaction. It is worth noting that the mechanism differs from the well-known blade–vortex interaction (BVI) that occurs on the main rotors of helicopters. In typical BVI the vortex axis and the blade span lie in almost parallel planes. For the most incriminated operational conditions the excitation by the oncoming vortex extends over a wide portion of the span. For the blade/tip–vortex interaction on CRORs, the plane tangent to the vortex helical path and the blade span are roughly perpendicular to each other. The impingement concentrates on the blade around the spanwise/radial location of the vortex path. This is why designing rear rotor blades with shorter tip radius than the front rotor blades, called clipping or cropping, is a possible way of avoiding or minimizing this interaction and the resulting noise. Nevertheless the interaction can have a residual level, either because of the extension of the vortex outer part or because of the contraction of the front-rotor stream tube. Furthermore side-winds or flight incidence possibly deflect tip vortices and make them interact with blade tips even in the presence of clipping. This justifies a specific address of the mechanism. The present contribution is a mathematical analysis dealing with two complementary aspects of vortex–airfoil interactions. The first aspect is the modeling of the tip–vortices shed from rotor blades for the sake of describing their subsequent impingement on downstream surfaces. The second one, specific to CRORs, is the effect of blade termination at the outer radius of a rear-rotor blade on the response of that blade to an oncoming front-rotor tip–vortex. In its final and complete form the addressed mechanism can then be referred to as blade–tip/tip–vortex interaction (BTTV).

Apart from CROR aeroacoustics, oblique and more general vortex–rotor interactions are encountered in rotorcraft technology, typically as the tip vortices generated by the main rotor of a helicopter are chopped by the tail rotor [1]. The generic problem of vortex impingement on an extended airfoil also possibly mimics the mechanism of noise production by interaction of blade–tip vortices with any downstream lifting surface of an airplane. This includes the interaction of the vortices shed by conventional pulling turboprops with the leading edge of a wing [2], or the interaction of the wake from a highly loaded CROR with a tail empennage. Because the associated tonal noise of installed propellers is seldom addressed in the literature, some interest has been found in providing physical insight into it; this is a secondary objective of the paper.

2. Methodology and problem statement

For thin blades operating in significantly disturbed flows and at the subsonic Mach numbers characteristic of take-off and landing regimes of CRORs, Ffowcs Williams and Hawkings' formulation of the acoustic analogy [3,4] states that the noise is essentially produced by unsteady lift forces distributed on the blades. These forces act as equivalent acoustic dipoles radiating in a homogeneous propagation medium. Once they are known the sound field is simply obtained from the background of linear acoustics, therefore the critical task is to determine the forces first. When dealing with open-rotor tonal noise the forces are periodic and can be simulated accurately by Computational Fluid Dynamics, for instance Unsteady Reynolds-Averaged Navier–Stokes methods [5–8]. This requires prohibitive computational resources. Fast-running analytical techniques are much more compatible with the need for repeated calculations in the context of optimization algorithms. The counterpart is that crude simplifications are often made of both the flow features and the geometry of the blades.

Now the lift dipoles of CROR tonal noise are coherent sources distributed over highly non-compact blades characterized by sweep, twist and variable chord. They interfere in a way that must be reproduced with minimum inaccuracy so that the noise estimates make sense. This accuracy requirement is beyond the performances of most existing analytical theories which state about the aeroacoustic response of rectangular flat-plates free of tip effects. The sound-generating flow disturbances such as wakes or tip vortices also need being properly described in a three-dimensional context. It appears that getting a physically consistent evaluation of the tonal-noise sources with analytical methods is much more challenging than describing the sources of broadband noise. Indeed the statistical description of randomly distributed sources is less subject to interference issues [9]. In a tonal-noise context it is essential to extend the analytical approach so that key features of the real design are accounted for in the blade model.

The present developments start from the linearized theory of thin flat-plate response to oncoming frozen disturbances. As an alternative to the approach proposed by Howe [10], they are basically similar to Amiet's theory of vortex–airfoil interaction [11], in which the impulsive noise produced by a single vortex chopping is derived in the time domain from a response function of the airfoil *via* inverse Fourier transform. In contrast the whole analysis is here made in the frequency domain because it is dedicated to periodic interactions. Vortex chopping is interpreted as pure variations of the angle of attack around zero mean loading. As a consequence vortex stretching at the leading-edge stagnation point and vortex deformation by induction of the blade circulation are ignored (see [12,13]). They are believed to be of minor importance for thin CROR blades because the radius of curvature of the leading edge is very small. In contrast assuming frozen oncoming vortices would produce wrong acoustic estimates for thick surfaces such as aircraft wings or helicopter blades [14]. Other problem statements taking into account the actual airfoil design are proposed for instance by Leppington and Sisson [15]. From another standpoint the interest of the present study is that it addresses the effect of airfoil span end on the unsteady aerodynamic response.

Despite their idealized character the developments are a first attempt to include tip vortices in an efficient methodology of CROR tonal noise prediction currently developed elsewhere for wake–interaction noise [16,17,7]. A similar approach based on a model of helical vortices is described by Kingan and Self [18]. The problem of the effect of blade termination on the response to incident disturbances was first considered by Roger and Carazo [16] and declined to the case of an incident Oseen's vortex by Roger and Schram [19] and by Roger et al. [20]. The present work extends and continues previous studies by including both arbitrary vortex angle and blade sweep angle. For the sake of checking the sensitivity to the description of the oncoming disturbances a so-called exponential-vortex model is also considered as alternative to Oseen's model. Finally a parametric study of the effect of radial distance between the vortex path and the blade tip is performed, in order to assess the benefit of clipping.

The analytical developments resort to a strip-theory approach, according to which a propeller blade and its surrounding are split into thin annuli. Each annulus is unwrapped for the sake of locally describing the interaction in Cartesian coordinates. The unsteady aerodynamic response of a blade segment is determined as if it was in a translating motion tangent to the real helical motion. This approach allows applying airfoil response functions based on the assumption of locally homogeneous flow conditions in both streamwise and spanwise directions, and at the same time introducing spanwise variations by changing the geometrical and aerodynamic parameters from one annular strip to another. Conventionally the analysis is restricted to a single strip centered on the radius of the tip–vortex path. Both the onset of unsteady lift and the far-field radiation are considered in a reference frame attached to an isolated blade segment, in order to provide a clear insight into the intrinsic contributions of vortex circulation, combined vortex and blade-chord angles, radial tip/vortex distance and other parameters to the radiation efficiency. The rotational motion of a blade segment and the description of the sound field in a stationary reference frame are out of the scope of the present paper.

The configuration of a CROR system with rotors of equal radii is shown in Fig. 1a. For analytical purpose, the impinged blade segment is approximated by a swept parallelogram of constant chord c defined perpendicular to the leading edge. It is featured by the gray surface in Fig. 1b and can be shifted along the spanwise direction y_2' in order to generate different configurations relative to the incident vortex. Two reference frames are introduced, with axes along the chordwise and spanwise directions y_1' and y_2', and along the streamwise and normal directions y_1 and y_2, respectively. Note that the relative stream is assumed along the y_1 direction for consistency. Coordinates made dimensionless by the half chord length $c/2$ and denoted by stars will also be defined for further derivations in Section 4. The complementary description in the unwrapped mid-plane of the strip is defined in Fig. 2 for the case of zero sweep $\psi = 0$. Sweep is introduced afterwards by making the airfoil rotate in the clockwise direction around the y_3-axis from the zero-sweep configuration.

Because the number of blades is moderate in the applications and the solidity is small at the tip, the response of a blade is not significantly influenced by the presence of adjacent blades; therefore isolated-airfoil response functions are considered. The latter are also best suited in the case of an impinged wing or empennage. The excitation of the blade segment, its aerodynamic response and the associated sound radiation are addressed in what follows as three distinct modeling steps. First the analytical vortex models and their gust expansions are detailed in Section 3 below. The aerodynamic response of a blade segment is discussed in Section 4 as if it had an infinite span. Yet the radiated sound is further calculated by

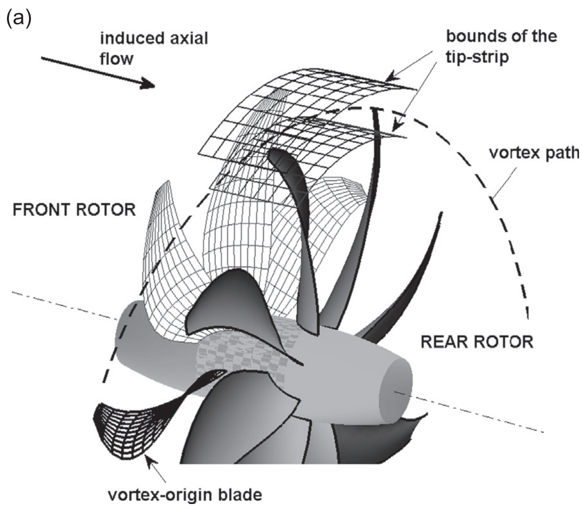

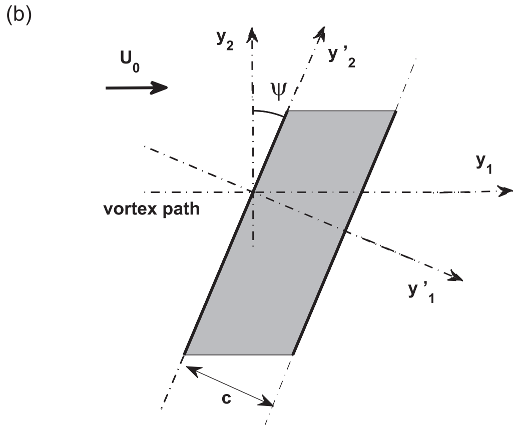

Fig. 1. (a) Schematic view of tip–vortex interaction in a CROR, featuring the tip annulus addressed in the model, case of equal radii. (b) Sets of coordinates attached to a swept blade–tip segment. Note that sweep is defined backward in the design of CRORs, in the clockwise direction in the axes (y_1, y_2).

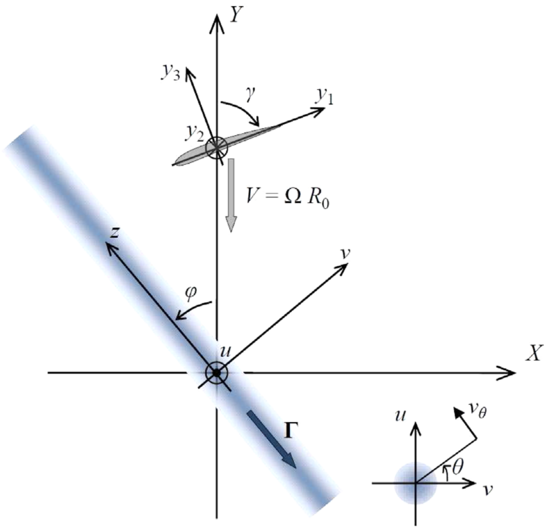

Fig. 2. Sets of coordinates for the statement of vortex–airfoil interaction with no sweep, from [19]. Non-zero sweep is introduced through additional airfoil rotation around the y_3-axis, according to Fig. 1b.

integrating the sources over the actual span for various vortex trajectories. The effect of the termination of the blade segment is accounted for by means of a tip correction derived in Section 5, where the sound radiation is re-considered. This allows pointing at not only the combined effects of vortex and blade features, but also the effect of the tip response, on the sound predictions.

3. Tip–vortex model

3.1. Gust expansion of model vortices—zero sweep

The blade/tip–vortex interaction is described first assuming zero sweep in this section, using the coordinate systems illustrated in Fig. 2. The selected strip for the analysis has the same mean radius as the helical path of the incident vortex. This radius will be taken as the origin of the spanwise coordinate y_2. For subsequent analyses, the blade–tip section will be considered at either positive or negative values of that coordinate. According to the linearized airfoil theory, the unsteady loads on a blade depend essentially on the normal velocity perturbation induced by the incoming vortex, expressed in the (y_1, y_2, y_3) coordinate system attached to the blade. It is assumed that the vortex diffusion takes place over distances which remain large when compared to the blade chord, so that the trace of a cylindrical line-vortex description is relevant in the unwrapped plane of coordinates (X, Y) with angle φ between the vortex axis and the tangential direction Y (Fig. 2). Any consistent vortex model combines a solid-body rotation core and some radial decrease of the tangential velocity profile in the outer region. The free-vortex Oseen model $V_\theta(r) = (\Gamma/r)[1-\mathrm{e}^{-(r/r_0)^2}]$, where $2\pi\Gamma$ and r_0 are the circulation and the core-radius parameter, respectively, is usually selected for its analytical tractability. Once projected in the reference frame of the considered blade segment, the corresponding upwash is written as

$$w(y_1, y_2, t) = -\Gamma\,\cos(\gamma+\varphi) y_2 \frac{1-\mathrm{e}^{-(y_2^2+\sin^2(\gamma+\varphi)[y_1-U_c t]^2)/r_0^2}}{y_2^2+\sin^2(\gamma+\varphi)[y_1-U_c t]^2} \tag{1}$$

introducing the phase speed $U_c = \sin\varphi\ V/\sin(\gamma+\varphi)$ along the chord line, where $V = \Omega R_0$ denotes the tangential speed of the blade segment relative to the vortex (R_0 is the mean radius of the considered strip and Ω the relative rotational speed). Though U_c does not coincide with the relative flow speed U_0 introduced in Fig. 1b, both will be assumed equal for the preliminary investigations achieved in the paper. γ is the stagger angle of the blades. Note that Amiet's analysis [11] is based on the same vortex model written differently as

$$V_\theta(r) = \left(1+\frac{1}{2a}\right)\frac{r_0}{r} v_0 \left[1-e^{-a(r/r_0)^2}\right]$$

where the value $a = 1.25643$ ensures that the maximum speed is exactly obtained for $r = r_0$.

Elementary blade/tip–vortex impingement is an impulsive mechanism, but its declination in the context of CRORs is periodic with the relative blade-passing period of the front rotor, noted T, as seen from the aforementioned reference frame. As such it can be analyzed in the frequency domain in the same way as what is currently done for wake–interaction noise in turbomachines. This choice is inherent to the unsteady aerodynamic model described later on in the paper. The time Fourier transform of the signal $w(y_1, y_2, t)$ according to the convention $\mathrm{e}^{-\mathrm{i}\omega t}$ for monochromatic waves and for positive frequencies is first derived as [21]

$$\tilde{w}(\omega) = \frac{1}{2\pi}\int_{-\infty}^{\infty} w(y_1, y_2, t)\,\mathrm{e}^{\mathrm{i}\omega t}\,\mathrm{d}t = -\frac{\Gamma\cot(\gamma+\varphi)\,\mathrm{e}^{\mathrm{i}k_1 y_1}}{4U_c}\left[h(-y_2) - h(y_2)\right] \tag{2}$$

with

$$h(y_2) = \mathrm{e}^{\mathrm{i}k_1 y_2/\sin(\gamma+\varphi)}\left[1 - \mathrm{erf}\left(\frac{k_1 r_0}{2\sin(\gamma+\varphi)} + \frac{y_2}{r_0}\right)\right]$$

and $k_1 = \omega/U_c$, erf denoting the error function. This is an odd function of y_2, as expected.

Another model vortex with a much faster exponential decay of the tangential velocity profile as $V_\theta(r) = A_0 r\mathrm{e}^{-r/r_0}$, A_0 being another constant, can be proposed as an alternative if the $1/r$ decay is considered abusively slow, even though it is incompatible with the definition of a non-zero circulation. It is worth noting that still another expression is proposed by George and Chou [1] as

$$V_\theta(r) = \frac{\Gamma}{r}\frac{r^2}{r^2 + r_0^2}$$

who also stressed that very similar acoustic signatures are produced by this model and the Oseen vortex velocity law. The three model expressions are compared in Fig. 3 where it is found that they produce similar velocity profiles around the maximum, thus similar descriptions of the vortex core, provided that the parameters are properly tuned. Helical vortex models dedicated to CRORs have been proposed by Kingan and Self [18]; they are not assessed here because the emphasis is on the local impact around the tip of an impinged blade. Only the Oseen and exponential models are retained later on. The lack of consistency of the exponential vortex is not an issue here because the analysis resorts to the velocity field and not to vorticity. Very different models are just the opportunity of assessing the sensitivity of the final trends with respect to the description of the vortices.

The upwash of the exponential vortex is written as

$$w(y_1, y_2, t) = -\cos(\gamma+\varphi)\,A_0 y_2 \mathrm{e}^{-\{y_2^2 + \sin^2(\gamma+\varphi)[y_1 - U_c t]^2\}^{1/2}/r_0} \tag{3}$$

and the time Fourier transform reads [21]

$$\tilde{w}(\omega) = \frac{-2A_0\cos(\gamma+\varphi)\,\mathrm{e}^{\mathrm{i}k_1 y_1}}{r_0\sqrt{\omega^2 + (\sin(\gamma+\varphi)U_c/r_0)^2}}\,y_2^2 K_1\left[y_2\sqrt{\left(\frac{1}{r_0}\right)^2 + \left(\frac{k_1}{\sin(\gamma+\varphi)}\right)^2}\,\right] \tag{4}$$

for $y_2 > 0$, where K_1 is the modified Bessel function. Since the cut through a vortex features antisymmetric signals and because negative arguments of K_1 lead to mathematical difficulties, the result for $y_2 < 0$ must be taken as the opposite of the one for $y_2 > 0$.

The spectral content of the impingement depends on the spanwise coordinate y_2. For the sake of deriving the induced unsteady loads from Schwarzschild's technique later on in the paper, the expression of the upwash must be now expanded in sinusoidal gusts in the spanwise direction, resorting to a space Fourier transform even though such a transform seems

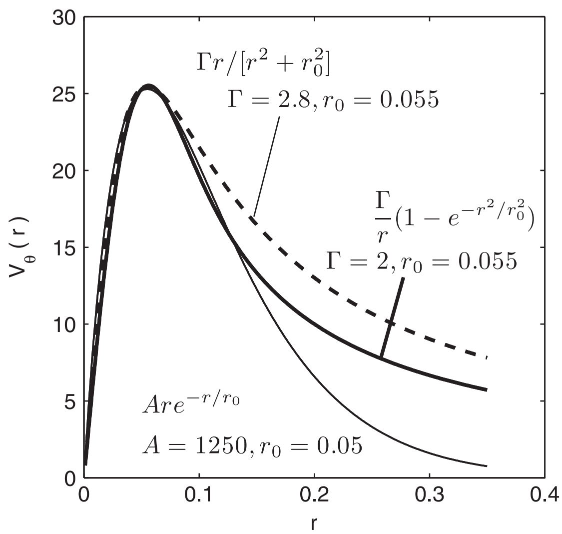

Fig. 3. Model tangential velocity profiles of the Oseen vortex (—), George and Chou's vortex (– –) and the exponential vortex (——). Model parameters indicated on the plots.

somewhat inappropriate for concentrated patterns:

$$\tilde{G}(k_1,k_2)=\frac{1}{2\pi}\int_{-\infty}^{\infty}\left[\tilde{w}(\omega)\mathrm{e}^{-\mathrm{i}k_1y_1}\right]\mathrm{e}^{-\mathrm{i}k_2y_2}\,\mathrm{d}y_2.$$

This finally provides the complex amplitude of the gust of wavenumbers (k_1,k_2) as [21]

$$\tilde{G}(k_1,k_2)=\frac{\mathrm{i}\Gamma k_2}{2\pi U_c}\cot(\gamma+\varphi)\frac{\mathrm{e}^{-r_0^2(k_2^2+[k_1/\sin(\gamma+\varphi)]^2)/4}}{k_2^2+[k_1/\sin(\gamma+\varphi)]^2} \tag{5}$$

for the Oseen vortex. Similarly the result for the exponential vortex is derived introducing the generic function $x^2\overline{K}_1(x)$ and its Fourier integral

$$\tilde{F}(k)=\frac{1}{2\pi}\int_{-\infty}^{\infty}x^2\overline{K}_1(x)\mathrm{e}^{-\mathrm{i}kx}\,\mathrm{d}x$$

with $\overline{K}_1(x)=K_1(x)$ for $x>0$ and $\overline{K}_1(x)=-K_1(-x)$ for $x<0$. The result is found as [21]

$$\tilde{F}(k)=\frac{\Gamma(4)\Gamma(2)}{\sqrt{\pi}\Gamma(7/2)}\left\{\frac{F\left(4,\frac{3}{2};\frac{7}{2};-\frac{1-\mathrm{i}k}{1+\mathrm{i}k}\right)}{(1+\mathrm{i}k)^4}-\frac{F\left(4,\frac{3}{2};\frac{7}{2};-\frac{1+\mathrm{i}k}{1-\mathrm{i}k}\right)}{(1-\mathrm{i}k)^4}\right\}$$

where F stands for the general hypergeometric functions. Note that here $\tilde{F}$ is a pure imaginary and odd function of its argument. The complex amplitude of the gust of wavenumbers (k_1,k_2) finally reads

$$\tilde{G}(k_1,k_2)=-\frac{2A_0}{r_0U_c}\cot(\gamma+\varphi)\frac{1}{Q^4}\tilde{F}\left(\frac{k_2}{Q}\right) \tag{6}$$

with

$$Q=\left[\left(\frac{1}{r_0}\right)^2+\left(\frac{k_1}{\sin(\gamma+\varphi)}\right)^2\right]^{1/2}$$

for $k_2>0$.

The algorithm for the hypergeometric functions is based on Gauss' series of Gamma functions [22]

$$F(a,b;c;Z)=\frac{\Gamma(c)}{\Gamma(a)\Gamma(b)}\sum_{n=0}^{\infty}\frac{\Gamma(a+n)\Gamma(b+n)Z^n}{\Gamma(c+n)\quad n!}.$$

The series converges only for $c>b+a$ and may feature some oscillations when the condition is approached. Therefore the values of a and b are reduced by making use of properties of contiguous hypergeometric functions. The present calculations rely on the following relationships to get $F(4,3/2;7/2;Z)$ [22]:

$$F(4,3/2;7/2;Z)=\frac{-(3-Z)}{8(Z-1)}F(2,3/2;7/2;Z)+\frac{5-3Z}{8(Z-1)^2}F(1,3/2;7/2;Z),$$

$$F(2,3/2;7/2;Z)=\frac{-6}{Z-1}F(2,-1/2;7/2;Z)+\frac{5-3Z}{Z-1}F(2,1/2;7/2;Z).$$

The wavenumber spectrum $\tilde{G}$ of the Oseen vortex is illustrated in Fig. 4. A qualitatively similar plot would be obtained for the exponential vortex. Depending on the relative values of the wavenumbers k_1 and k_2, two sets of gusts are defined. When $k_2>M_0k_1/\beta^2$, the gust is said to be sub-critical; otherwise it is said supercritical. The meaning of this notion is discussed in Section 4.1. The transition between the ranges of sub-critical and supercritical gusts is featured by the vertical grid-plane in the figure. It is remarkable that more energy is distributed in the sub-critical range.

3.2. Periodic interaction in open-rotor architecture

The periodic impingement of successive tip vortices is simply reproduced by duplicating the previously derived solutions *via* an infinite series, according to the convolution product

$$f_W(t)=\sum_{n=-\infty}^{\infty}w(y_1,y_2,t-nT)=w(y_1,y_2,t)*\sum_{n=-\infty}^{\infty}\delta(t-nT)$$

with $T=2\pi R_0/(BV)$, where B is the number of blades. The resulting signals for the two investigated model vortices are shown in Fig. 5. Despite the difference in the description of a single vortex, combining a series of vortices to simulate the periodic interaction provides very similar velocity profiles in the present case. This suggests that selecting one model or the other one makes negligible differences. Nevertheless both are detailed in this study for completeness. The figure also compares the model tangential velocity profiles to numerical predictions based on Unsteady RANS simulations, achieved on a full open-rotor architecture [23]. The radial velocity is extracted at two different axial locations from the numerical mesh, as the most representative quantity for the tip vortex. The negative mean-value of the profiles is attributed to the

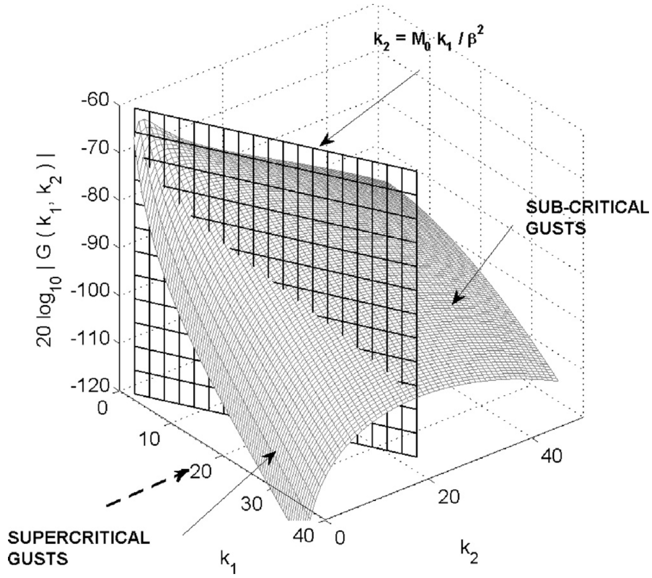

Fig. 4. Two-dimensional gust-wavenumber spectrum of the incident upwash of the Oseen vortex impinging on a rectangular unswept blade. See Section 4.1 for definitions. Parameters: $\gamma=25^{\circ}$, $\varphi=20^{\circ}$, $V=300$ m/s, $r_0=5$ cm, $\Gamma=4\,\mathrm{m}^2$/s. The value of the blade passing frequency (BPF) chosen for illustration in Fig. 9 is shown by the dashed arrow.

contraction of the stream tube of the front rotor. The model profiles nicely recover a part of the numerical results, at least for the shortest downstream distance of 0.3 chord length. Some asymmetry is found in the simulated patterns, departing from the analytical models. This asymmetry increases farther downstream. It is attributed to the dynamics of the vortex and more precisely its coupling with the complementary accelerations induced by the swirl of the front rotor. The comparison confirms that the aforementioned models are physically consistent but that they should be improved to include swirl-induced asymmetry in a future work. The velocity profiles could also be taken directly from the simulations to provide alternative, numerical values of the function $\tilde{G}(k_1,k_2)$.

The Fourier series

$$\tilde{f}_W(\omega)=\sum_{n=-\infty}^{\infty} f_n\delta(\omega-n2\pi/T) \quad \text{with } f_n=\frac{2\pi}{T}\tilde{w}\left(\frac{2\pi}{T}\right)$$

of a periodic vortex train selects discrete frequencies in practical applications. Therefore simply addressing the interaction at a single frequency from any expression of $\tilde{w}$ makes sense. Within the scope of a complete modeling of open rotors, the gust-splitting of a series of vortices would be used to derive first the unsteady loads on a blade–tip segment. The segment would be discretized as a set of patches and the far-field radiation calculated applying Hanson's formulation [24] or the equivalent implementation derived by Carazo et al. [17]. The declination of the model in a rotating-blade configuration is beyond the scope of the paper.

4. Infinite-airfoil response functions

The response of an infinite-span airfoil to arbitrary incident gusts is formulated in this section in the general configuration of Fig. 1b. With respect to the axes (y_1',y_2'), sweep is equivalent to a non-zero spanwise component U_2 of the incident flow speed. From this general framework the response of an unswept airfoil follows by just setting $U_2=0$.

4.1. Expressions of the unsteady lift

Consider the sinusoidal, normal-velocity gust $\mathbf{w}(y_1',y_2',t)=w_0(k_1',k_2')\exp\{\mathrm{i}(k_1'y_1'+k_2'y_2'-\omega t)\}\mathbf{e}_3$, convected over the airfoil at the oblique speed $\mathbf{U_0}=U_1\mathbf{e_1}+U_2\mathbf{e_2}$. The impingement of the gust generates a potential velocity disturbance $\mathbf{u}'=\nabla\phi'$ such that ϕ' is solution of the general convected Helmholtz equation

$$\beta_1^2\frac{\partial^2\phi'}{\partial y_1'^2}+\beta_2^2\frac{\partial^2\phi'}{\partial y_2'^2}+\frac{\partial^2\phi'}{\partial y_3'^2}+2\mathrm{i}k\left(M_1\frac{\partial\phi'}{\partial y_1'}+M_2\frac{\partial\phi'}{\partial y_2'}\right)$$

$$-2M_1M_2\frac{\partial^2\phi'}{\partial y_1\,\partial y_2}+k^2\phi'=0 \tag{7}$$

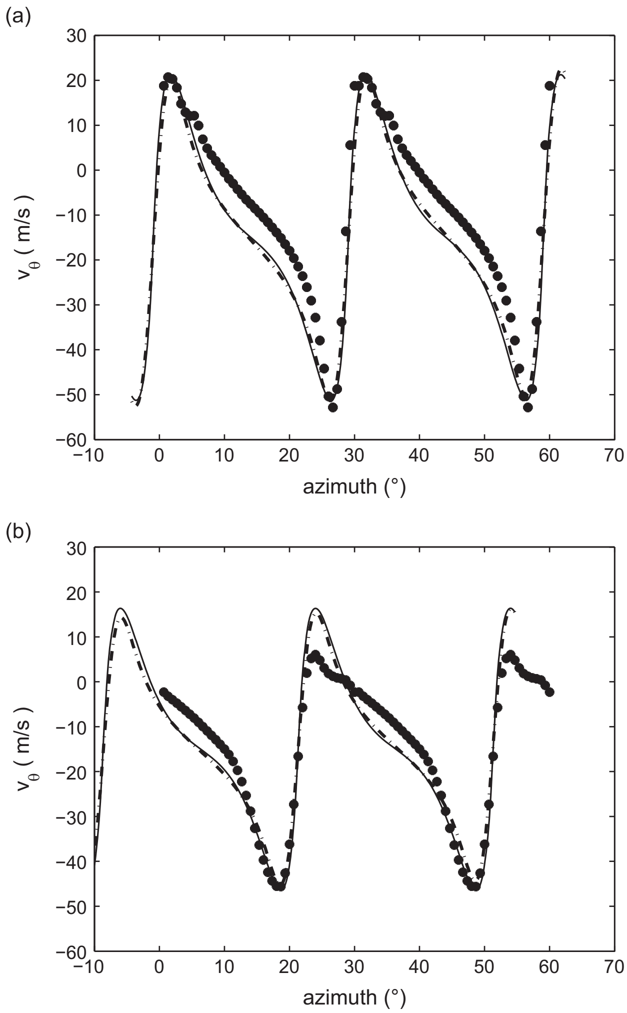

Fig. 5. Compared periodic tip–vortex velocity profiles according to Oseen's vortex model (–·–), exponential vortex model (——) and URANS computations (•) [23]. (a) 30 percent chord downstream; (b) 50 percent chord downstream. Parameters: $(\Gamma, r_0) = (1.5\ \mathrm{m^2/s}, 2.5\ \mathrm{cm})$, $(A, r_0) = (3700\ \mathrm{s^{-1}}, 2.7\ \mathrm{cm})$.

with $k = \omega/c_0$, $\beta_1 = \sqrt{1-M_1^2}$, $\beta_2 = \sqrt{1-M_2^2}$, M_1 and M_2 being the chordwise and spanwise Mach numbers, respectively. The boundary conditions on $y_3 = 0$ are the cancellation of the potential upstream of the leading edge ($y_1' < 0$), the cancellation of the normal velocity on the airfoil surface ($0 < y_1' < c$) and the Kutta condition at the trailing edge and downstream ($y_1' > c$). Since no condition is imposed along the coordinate y_2, the disturbance potential is sought according to the incident gust obliqueness as $\phi' = \phi(y_1', y_3)\mathrm{e}^{\mathrm{i}(k_2' y_2' - \omega t)}$, so that the reduced convected Helmholtz equation on ϕ is obtained as follows:

$$\beta_1^2 \frac{\partial^2 \phi}{\partial y_1'^2} + \frac{\partial^2 \phi}{\partial y_3^2} + 2\mathrm{i}\left(kM_1 - M_1 M_2 k_2'\right)\frac{\partial \phi}{\partial y_1'} + \left(k^2 - k_2'^2 \beta_2^2 - 2M_2 k k_2'\right)\phi = 0. \tag{8}$$

This leads to the canonical Helmholtz equation for the transformed velocity potential $\Phi = \phi(y_1'^*, y_3^*)\mathrm{e}^{\mathrm{i}M_1^2 k_1'^* y_1'^* / \beta_1^2}$ once the coordinates and wavenumbers are made dimensionless by $c/2$ (superscript $*$):

$$\frac{\partial \Phi}{\partial y_1'^{*2}} + \frac{\partial \Phi}{\partial y_3^{*2}} + \kappa^2 \Phi = 0, \tag{9}$$

where

$$\kappa^2 = \frac{k_2'^{*2}}{\beta_1^4}\left(\frac{M_1^2}{\sin^2\alpha} - 1\right) = \mu^2\left[1 - \frac{1}{\Theta^2}\right], \quad \Theta = \mu\beta_1 / k_2'^*$$

with $\mu = k_1^{'*} M_1/\beta_1^2$, $k_1^{'*} = K\cos\alpha$ and $k_2^{'*} = K\sin\alpha$, introducing the gust skewness angle α and the total non-dimensional aerodynamic wavenumber $K = |\mathbf{K}|$ such that $\omega c/2 = \mathbf{U}_0 \cdot \mathbf{K} = U_1 k_1^* + U_2 k_2^* = U_0 k_1^*$ with $k_1^* = K\cos(\alpha - \psi)$. Θ is known as Graham's parameter [25].

Schwarzschild's theorem [26] aimed at solving Eq. (9) with the boundary conditions

$$\Phi(y_1^{'*}, 0) = f(y_1^{'*}), \quad y_1^{'*} > 0,$$

$$\frac{\partial \Phi}{\partial y_3^*}\Big|_{y_3^* = 0} = 0, \quad y_1^{'*} < 0,$$

where f is a known function, states that the trace of the potential on the complementary half-space $y_1^{'*} < 0$ reads

$$\Phi(y_1^{'*}, 0) = \frac{1}{\pi}\int_0^\infty (-y_1^{'*}/\xi)^{1/2}\left[1/(\xi - y_1^{'*})\right] e^{i\kappa(\xi - y_1^{'*})} f(\xi, 0)\, d\xi.$$

Amiet's method [27] is based on the iterative use of this theorem to determine the unsteady lift due to an incident gust, each iteration accounting for the contribution of one edge. The impingement of the incident gust at leading edge is first interpreted as a problem of wave scattering by the edge of a rigid half-plane. A zero-order disturbance potential which would cancel the normal velocity $\mathbf{w}$ over the entire plane $y_3 = 0$ is introduced as initial solution [28]. Then the dominant leading-edge scattering is derived by adding a first-order potential ensuring the condition of no flow across the surface $(y_3 = 0, y_1^{'} > 0)$, and canceling the initial potential on $(y_3 = 0, y_1^{'} < 0)$. This step is achieved by Schwarzschild's theorem, and the resulting first approximation of the solution $\Phi_1(y_1^{'*}, 0)$ yields the corresponding lift or pressure-jump surface density, expressed as

$$\tilde{\ell}_1\left(k_1^{'*}, k_2^{'*}\right) = \frac{-2\rho_0 U_1 w_0 e^{i\pi/4}}{\sqrt{\pi(k_1^{'*} + \beta_1^2\kappa) y_1^{'*}}} e^{-i(\mu M_1 - \kappa) y_1^{'*}} e^{i k_2^{'*} y_2^{'*}} e^{-i\omega t}. \tag{10}$$

This quantity is twice the disturbance pressure, since the pressure fluctuations have opposite phases on both sides. In a second step the solution is corrected by a second-order term $\tilde{\ell}_2$ which cancels $\tilde{\ell}_1$ at the trailing-edge and beyond in order to fulfill a perfect Kutta condition. The correction is derived by writing down another Schwarzschild's problem for the pressure jump on the half-plane $(y_3 = 0, y_1 > c)$, accepting some approximation in the integral [28], as

$$\tilde{\ell}_2\left(k_1^{'*}, k_2^{'*}\right) = \frac{2\rho_0 U_1 w_0 e^{i\pi/4}}{\sqrt{2\pi(k_1^{'*} + \beta_1^2\kappa)}} \times \left[1 - (1+i)E^*\left[2\kappa(y_1^{'*} - 2)\right]\right] e^{-i(\mu M_1 - \kappa) y_1^{'*}} e^{i k_2^{'*} y_2^{'*}} e^{-i\omega t}, \tag{11}$$

E being the Fresnel integral introduced by Amiet

$$E(x) = \int_0^x \frac{e^{i\xi}}{\sqrt{2\pi\xi}}\, d\xi$$

and the asterisk denoting the complex conjugate, with the property that $E(-x) = iE^*(x)$ and $E^*(-x) = -iE(x)$. The total aerodynamic response of the airfoil is given by $\tilde{\ell} = \tilde{\ell}_1 + \tilde{\ell}_2$. It must be noted that Eqs. (10) and (11) have been first derived by Adamczyk using the Wiener–Hopf technique [29]. They hold for supercritical gusts such that $\kappa^2 > 0$. The case of the sub-critical gusts is easily found by using the modified value $i\kappa' = i\sqrt{-\kappa^2}$ instead of κ, and replacing the square bracket involving the Fresnel integral E^* by the term $1 - \mathrm{erf}([2\kappa'(1 - y_1^{'*})]^{1/2})$ involving the error function. The simplified expressions for oblique gusts impinging on an unswept airfoil are simply obtained by considering zero sweep $\psi = 0$. They are found equivalently by Mish and Devenport [30], Moreau et al. [31] and Roger [32]. The complete solution is not sensitive to the exact behavior of the correction $\tilde{\ell}_2$ far upstream from the trailing edge, where the lift is dominated by the leading-edge inverse square-root singularity. For a better two-dimensional representation of the lift distribution over the airfoil, the quantity $\tilde{\ell}\sqrt{y_1^{'*}}$ referred to as the 'regularized lift' will be chosen subsequently.

Sub-critical gusts are characterized by a faster drop of the unsteady lift downstream from the leading edge because of the factor $e^{-\kappa' y_1^{'*}}$. They also radiate less efficiently for spanwise-distributed sources and their actual contribution in vortex–airfoil interaction noise is a point of interest. In the test case of Fig. 4 the dominant hump of the function precisely enters the range of sub-critical gusts. Furthermore gust–airfoil interactions at relatively high frequencies take place well beyond the maximum energy of the wavenumber spectrum. This is expected for instance for most combination tones produced by tip–vortex interactions on CRORs.

4.2. Blade response without tip correction – zero sweep

The unsteady lift locally induced on an airfoil of arbitrary large span and zero sweep by an incident Oseen vortex is shown in Fig. 6 for both the supercritical and sub-critical gusts as well as their combination. Sub-critical gusts appear to contribute substantially more than supercritical gusts. Both sets produce extended traces when separated whereas their combined effect results in a more concentrated trace featuring an upwash–downwash pattern, at least as long as the

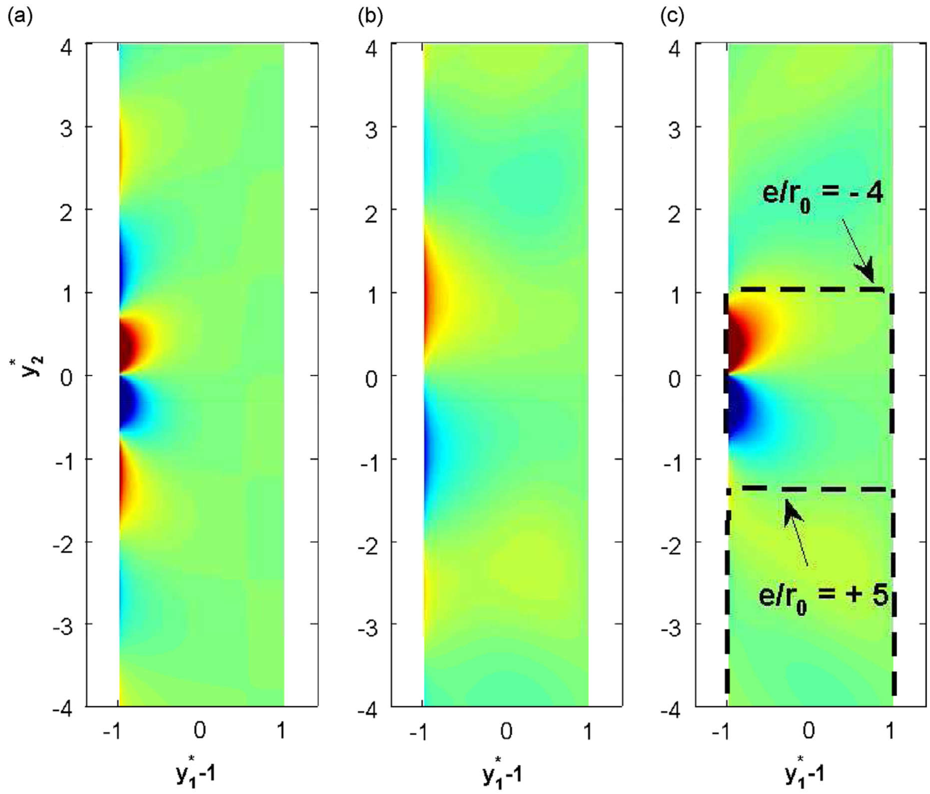

Fig. 6. Colormap of the instantaneous lift produced by all oblique gusts contributing to a given wavenumber $\mu = 2.7$ on a rectangular airfoil, ignoring tip effects. (a) Sub-critical; (b) supercritical; (c) total. $M_0 = 0.54$, flow from left to right, vortex axis at mid span, vortex core size $r_0 = c/8$. Dashed lines: limit tip positions considered in Fig. 7. Singular leading-edge vicinity removed, arbitrary scale. (For interpretation of the references to color in this figure caption, the reader is referred to the web version of this article.)

interaction takes place on an airfoil of large spanwise extent, far from the span ends. The pattern acts as two dipoles with opposite phases that are likely to produce some cancellation in the acoustic radiation field. This situation is not likely to occur on CRORs because the impingement of front-rotor tip vortices contaminates the tip section of a rear-rotor blade. Yet it has to be considered if the model is also used to describe the impingement of a puller–propeller wake onto the leading edge of a wing or of a tail empennage. Furthermore, even though the design of a CROR involves clipping to avoid the blade/tip–vortex interaction, operating conditions at take-off or landing are accompanied with significant contraction of the front-rotor stream tube that possibly re-activates this interaction. In normal clipping conditions only a part of the incident vortex impinges on the blade. In the special case of vortex axis impinging exactly at the blade–tip radius, only one-half of the pattern in Fig. 6 produces sound. A relatively high acoustic signature is expected, not only because of the amplitude of the impingement but also because of the absence of cancellation between downwash and upwash contributions. This sensitivity will be addressed in Section 4.3.

Analytical modeling of BTTV *a priori* requires a proper account of both sub-critical and supercritical gusts, on one hand, and a tip correction of the blade response, on the other hand. But the main expected effect of the blade termination is the truncation of the localized unsteady lift pattern with respect to the distributions of Fig. 6, which possibly deactivates or redefines the aforementioned cancellation. The tip correction can be first ignored in order to focus on the intrinsic properties of the cancellation. This means that classical Amiet's theory and the expressions (10) and (11) can be used as such to describe the unsteady lift acting as sources. In contrast the radiation efficiency of the interaction is assessed by integrating the sources over the actual wetted surface. For an observer in the acoustic and geometric far-field and a spanwise extent $L = 2d$ centered at $y_2^* = 0$, the contribution of a gust is known as

$$\tilde{p}(\mathbf{x},\omega) = \frac{-kc\rho_0 x_3}{2S_0^2} U_0 \, d\tilde{w} \, \frac{\sin[d(k_2 - kx_2/S_0)]}{d(k_2 - kx_2/S_0)} \mathcal{I}$$

introducing the chordwise aeroacoustic transfer function $\mathcal{I}$. Here the convection-corrected distance $S_0 = [x_1^2 + \beta^2(x_2^2 + x_3^2)]^{(1/2)}$ is introduced, with $\beta = \sqrt{1 - M_0^2}$ and $M_0 = U_0/c_0$, $\mathbf{x} = (x_1, x_2, x_3)$ being observer's coordinate vector. The coordinates are defined along the chord, along the span and normal to the airfoil plane, respectively, with origin at the airfoil center point. The precise location of the origin in the source domain makes no difference in the underlying acoustic and geometric far-field approximation. For supercritical gusts the full expression of $\mathcal{I}$ is the sum of two terms [32] $\mathcal{I}=\mathcal{I}_1+\mathcal{I}_2$ with

$$\mathcal{I}_1=-\frac{1}{\pi}\sqrt{\frac{2}{(k_1^*+\beta^2\kappa)\Theta_4}}\,\mathrm{e}^{-\mathrm{i}\Theta_2}E[2\Theta_4], \tag{12}$$

$$\mathcal{I}_2=\frac{\mathrm{e}^{-\mathrm{i}\Theta_2}}{\pi\sqrt{2\pi(k_1^*+\beta^2\kappa)\Theta_4}}\times\left\{\mathrm{i}\left(1-\mathrm{e}^{2\mathrm{i}\Theta_4}\right)-(1+\mathrm{i})\left[E(4\kappa)-\mathrm{e}^{2\mathrm{i}\Theta_4}\sqrt{\frac{2\kappa}{\Theta_3}}E[2\Theta_3]\right]\right\}, \tag{13}$$

and $\Theta_2=\mu(M_0-x_1/S_0)-\pi/4$, $\Theta_3=\kappa+\mu x_1/S_0$, $\Theta_4=\kappa-\mu x_1/S_0$.

For sub-critical gusts the expressions follow as

$$\mathcal{I}_1=-\frac{1}{\pi}\sqrt{\frac{2}{(k_1^*+\mathrm{i}\beta^2\kappa')\Theta_4'}}\,\mathrm{e}^{-\mathrm{i}\Theta_2}E\left[2\Theta_4'\right], \tag{14}$$

$$\mathcal{I}_2=\frac{-\mathrm{e}^{-\mathrm{i}\Theta_2}}{\mathrm{i}\pi\sqrt{2\pi(k_1^*+\mathrm{i}\beta^2\kappa')\Theta_4'}}\times\left\{1-\mathrm{e}^{2\mathrm{i}\Theta_4'}-\mathrm{erf}\left(\sqrt{4\kappa'}\right)+2\mathrm{e}^{\,2\mathrm{i}\Theta_4'}\sqrt{\frac{\kappa'}{\Theta_3'}}E\left[2\Theta_3'\right]\right\}, \tag{15}$$

with $\Theta_4'=\mathrm{i}\kappa'-\mu x_1/S_0$, $\Theta_3'=\mathrm{i}\kappa'+\mu x_1/S_0$.

If the spanwise radiation integral is calculated from $-d$ to $-e$ in order to account for a blade tip located at some distance e from the vortex axis, e being positive for a vortex passing beyond the tip, the sine cardinal function must be replaced by

$$\frac{\mathrm{e}^{-\mathrm{i}(k_2-kx_2/S_0)e}-\mathrm{e}^{-\mathrm{i}(k_2-kx_2/S_0)d}}{\mathrm{i}(k_2-kx_2/S_0)d} \tag{16}$$

4.3. Effect of radial tip–vortex distance and directivity considerations

Classical Amiet's theory together with Eq. (16) for the span-wise integral provides a simplified way of assessing the effect of the distance of the vortex path to the blade tip on the acoustic radiation. Part of this effect is the truncation of the source distribution in the resulting interference. It is determined here by considering a rectangular airfoil of aspect ratio $L/c=2.5$ at different relative positions with respect to the vortex path. The impingement location e relative to the tip is defined in the reference frame of the airfoil, from $-4r_0$ to $5r_0$ where r_0 is the vortex core radius; the limits are shown in Fig. 6. The core radius to chord length ratio is $r_0/c=1/8$. For each configuration the far-field directivity diagram is integrated to provide an equivalent power level. Typical directivity diagrams are shown in Fig. 7(top) for the values $e/r_0=-4$ and 0 and the acoustic power is reported as a function of e/r_0 in Fig. 7(bottom). Whenever the impingement takes place far enough from the tip for the vortex signature of Fig. 6 be covered by the spanwise extent of the segment, the directivity diagram exhibits four lobes inclined at 45°. No sound is radiated in directions normal to the blade surface. This behavior holds for the left-hand side part of the plot of Fig. 7(bottom) where $e/r_0<-2$. The unsteady-lift pattern radiates like a lateral quadrupole because the downwash and upwash contributions tend to cancel each other as two opposite dipoles. As the vortex-path radius gets closer to the tip (typically $-2<e/r_0<-0.5$) one of the half patterns does not fully interact with the surface anymore. Globally the sound increases because the cancellation becomes less effective. At the special relative position $e/r_0=0$ no cancellation is possible and only one upwash or downwash dipole radiates. This is the condition of maximum sound. Finally for a vortex passage beyond the tip ($e/r_0>0$), the tip only experiences residual lift fluctuations associated with the outer part of the vortex. The sound progressively drops.

At the condition $e/r_0=0$ two broader directivity lobes are observed in the present example. The maximum radiation occurs at oblique inward directions but a significant sound is also emitted normal to the blade. The lobe inclination is similar to the cardioid directivity of trailing-edge noise, the blade tip section acting somewhat like the edge of a large plate. Because the characteristic lobes of the off-tip impingement are much thinner than the ones of the on-tip impingement, the acoustic power is larger for the latter than for the former. It has also been observed that the sound decreases keeping the same directivity as the parameter e/r_0 is increased from 0.

Because of its different velocity profile, the exponential vortex is found to exhibit a slightly faster sound decay with increasing interaction distance when compared to the Oseen vortex. Globally a 8 dB reduction relative to the maximum sound is achieved for a distance of 4 vortex-core radii. Yet it is found that even for a vortex path significantly beyond the tip the induction of unsteady lift around the tip is not negligible.

The overall features of both the induced lift and the acoustic radiation are similar for the two investigated model vortices. This suggests that the finest details of the vortex profile do not question the underlying physics of the interaction mechanism. Therefore only the Oseen vortex is retained later on in the paper, for the sake of simplicity.

The basic directivity in the reference frame of the impinged segment is only partly transposable to a full rotor. Indeed tonal rotor-noise directivity is imposed not only by source intrinsic features but also by blade-to-blade interference that is not considered in the present study. A rotor is equivalent to a phased circular array of moving blade segments. Extinction on the axis is predicted for inward impingement whatever the interference could be, corresponding to the zero sound in the

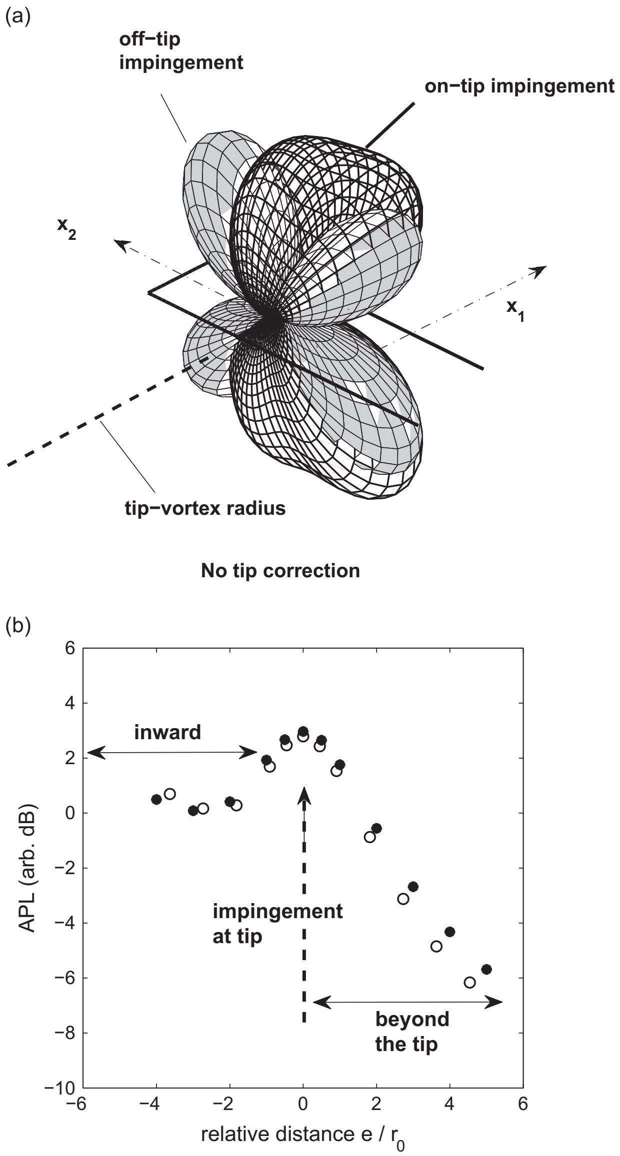

Fig. 7. Top: typical far-field directivity patterns of the sound radiated by vortex impingement onto a blade segment with zero sweep, ignoring tip correction. Oseen vortex, values of e/r_0 −4 and 0. Bottom: effect of relative vortex-to-tip distance on the radiated acoustic power. Oseen vortex (•) and exponential vortex (○), rectangular blade of aspect ratio $L/c = 2.5$, vortex core size $r_0 = c/8$.

plane (x_1, x_3), but the same extinction could be achieved by the interference. Nevertheless for small blade angles γ a local minimum is expected in the rotor plane because of the extinction in the plane (x_1, x_2), on the one hand, and different directivity patterns should be observed for inward and on-tip impingements, on the other hand.

Few experiments that could be used to assess the model predictions in terms of directivity are available in the literature. The work reported by Ahmadi [33] is referred to in this section to point out some difficulties in the definition of a reliable protocol. In the experiment a stationary tip vortex is produced by a rectangular airfoil of a large aspect ratio positioned vertically at the nozzle exit of an open-jet anechoic wind tunnel and partly immersed in the flow. A two-bladed rotor is mounted farther downstream with its axis aligned horizontally with the mean flow. The blade chord length is 6 cm and the rotor tip radius is 0.3 m. The vortex enters the rotor disk following the mean stream tube. Therefore the interaction is purely periodic and generates a series of tones at harmonics of the rotor blade-passing frequency. The effect of vortex chopping has been found to increase the baseline acoustic signature of the rotor, especially at higher harmonics, with minimum noise in the plane of the rotor. In contrast low-order harmonics can be discarded because they are not modified by the presence of the vortex. Sound is measured in the horizontal meridian plane of the rotor, by microphones distributed over an arc of radius 1.5 m. The investigated range is $[-40^\circ, 40^\circ]$, the zero angle being at the rotor plane.

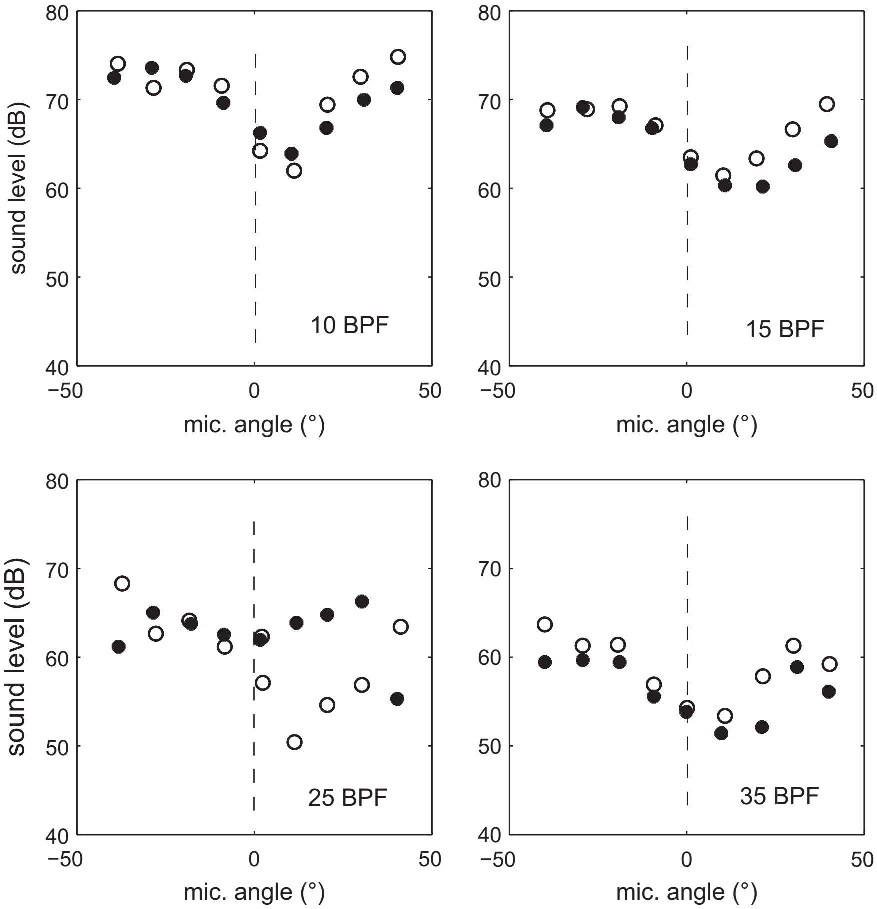

Fig. 8. Directivity diagrams at various higher BPF harmonics in Ahmadi's experiment [33]. $e/r_0 = -4$ (○), $e/r_0 = -1$ (•). Tip Mach number 0.59. Rotor-plane angle featured by the vertical dashed line.

Sample results are reproduced from the reference in Fig. 8. The selected operation point corresponds to a blade tip Mach number of 0.59 and an axial-flow speed of 8.2 m/s. The blade-passing frequency (BPF) is around 210 Hz. Sound levels are reported at four BPF high-order harmonics for which the baseline acoustic signature is negligible, in two configurations corresponding to the values -1 and -4 of the parameter e/r_0. As shown in Fig. 7, the case $e/r_0 = -4$ is characterized by the quadrupole-like directivity, whereas the case $e/r_0 = -1$ approaches the dipole-like behavior of tip impingement. The ratio $r_0/c = 1/7.5$ is close to the one assumed in the model predictions.

Precise quantitative comparisons are made questionable because of several issues. First, the tested airfoil is a NACA-0012 representative of helicopter main rotors whereas the present work is rather dedicated to much thinner blade–tip cross sections of CRORs. The local vortex dynamics is very sensitive to airfoil thickness at leading edge and all associated nonlinear effects are ignored in the analytical model. According to Ahmadi [33] the interaction also generates a drag dipole the axis of which is aligned with the blade chord; this is not covered by the analytical problem statement. Secondly, shifting the vortex impingement radius in the experiment from $e/r_0 = -1$ to $e/r_0 = -4$ also induces additional noise because the wake of the vortex generator interacts more significantly with the rotor blade tips. More precisely the measurements combine wake–interaction noise and tip–vortex impingement noise in such a way that the latter cannot be accurately extracted. Other concerns arise from the geometrical arrangement. The blade inclination angle γ of 9° in the experiment combines with the value $\varphi = \pi/2$, so that the equivalent upwash is proportional to $\cos(\varphi+\gamma) = -\sin\gamma$. Vortex chopping is not very efficient in these conditions according to the model. Furthermore the microphone distance and positioning are equivalent to an angular shift of 12° with respect to the plane (x_1, x_3) of Fig. 7(left). The dominant lobes of the interaction are not accessible, whereas the different directivity of wake–interaction noise possibly makes it more effective in the data. Finally the present vortex model ignores the wake-like velocity deficit in the direction of the vorticity vector which is expected in a real tip vortex. Keeping all aforementioned issues in mind, Fig. 8 globally confirms the dipole-like character of the measured sound with a local extinction in the rotor plane, featured by the vertical dashed lines, except for the harmonic order 25. Blade-to-blade interference is probably weak because the rotor has only two blades and the chopping is a very localized mechanism. The results also suggest that near-tip impingement ($e/r_0 = -1$) generates the same amount of noise or a couple of dB less than inward impingement ($e/r_0 = -4$), which is opposite to the expected trend. However wake–interaction with the vortex generator contaminates the measurements at $e/r_0 = -4$, as specially as the blade–tip segment is the most efficient acoustic source because of its highest speed, in such a way that the tip–vortex signature is overestimated. Taking this into account makes the present predictions compatible with experimental evidence.

It is worth noting that the design of a reliable validation experiment dedicated to blade–tip vortex interaction noise is a somewhat challenging task. The only convincing approach would be coupling the present model and a similar wake–interaction noise model within the scope of a full rotating-blade simulation, and comparing the model predictions with or without tip–vortex contribution to experimental data from a real CROR testing. Indeed because the combination tones produced by the interaction differ from the usual BPF harmonics of isolated rotors (at least for rotors designed with different blade numbers), the measurements would not be contaminated by extraneous source mechanisms, except the *a priori* negligible potential interaction. Such a task is not addressed here.

4.4. *Effect of blade sweep*

Because sweep is defined in the present problem from the unswept blade configuration $\psi = 0$ by making the segment rotate in its plane around the y_3-axis, the equivalent upwash defined by vortex intersection is kept unchanged. The only effect of sweep is to redefine the components of the aerodynamic wavenumber vector in the new axes (y_1', y_2'). The amplitude of a given gust, say $\tilde{G}(k_1, k_2)$, according to the expressions of Section 3.1 still holds for the same gust now expressed as a function of the vector of modified wavenumbers $\tilde{G}'(k_1', k_2')$. This is equivalent to rotate the pattern of the wavenumber spectrum already introduced in Fig. 5, as emphasized in Fig. 9. Both wavenumber vectors are related by

$$k_1 = \cos\,\psi k_1' + \sin\,\psi k_2', \quad k_2 = -\sin\,\psi k_1' + \cos\,\psi k_2'.$$

The set of gusts contributing to a given interaction frequency is indicated in each sub-plot of Fig. 9 by the thick dashed-dotted lines. In the presence of sweep this triggers a continuous range of values of the chordwise wavenumber. It is worth noting that in the plot of Fig. 9b the threshold between supercritical and sub-critical gusts is at a slightly smaller angle than in Fig. 9a, namely atan(M_1/β_1) instead of atan(M_0/β). But the aperture angle reduction is much less than the rotation of the map by the sweep angle ψ. More energy is transferred into the supercritical range from the negative spanwise wavenumbers (lower, labeled (-) part of the spectrum).

An example of loading distribution due to vortex impingement at mid-span of an airfoil of a large aspect ratio is shown in Fig. 10. The left-hand side plot refers to a zero-sweep configuration similar to that of Fig. 6. The right-hand side one refers to a sweep angle of 20°. The incident flow speed U_0 and the vortex parameters are the same in both plots. The plotted quantity is the regularized lift introduced in Section 4. As expected the loading distribution is symmetric for the zero-sweep case and asymmetric for the swept airfoil.

More generally the effect of sweep depends on the nature of the excitation by incident disturbances. For spanwise distributed excitations which would be nearly in phase along an unswept span, sweep would reduce the trace speed of the interaction along the leading edge. For the present case of concentrated impingement free of spanwise drift sweep favors higher trace speeds towards the tip (upper part of the plot in the figure), when compared to the zero-sweep case. In other

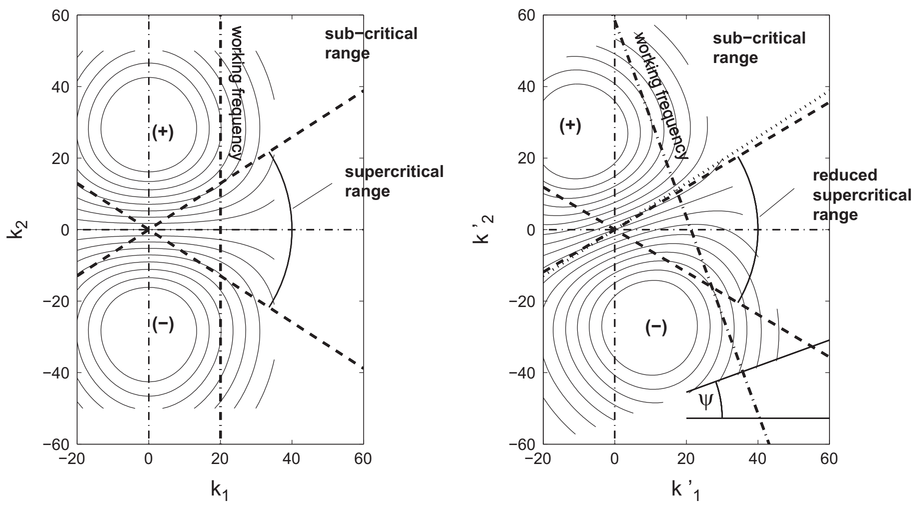

Fig. 9. Definition of sub-critical and supercritical ranges in the plane of chord-wise and span-wise wavenumbers. The iso-contour plot with (+) and (−) humps qualitatively illustrates the imaginary part of the spectrum $\tilde{G}(k_1, k_2)$. (a) Case of zero-sweep airfoil. (b) Swept airfoil. The same frequency corresponding to the value $k_1 = 20$ of the zero-sweep case is indicated by thick dashed-dotted lines on both plots. Critical limit of the unswept case repeated as the dotted line.

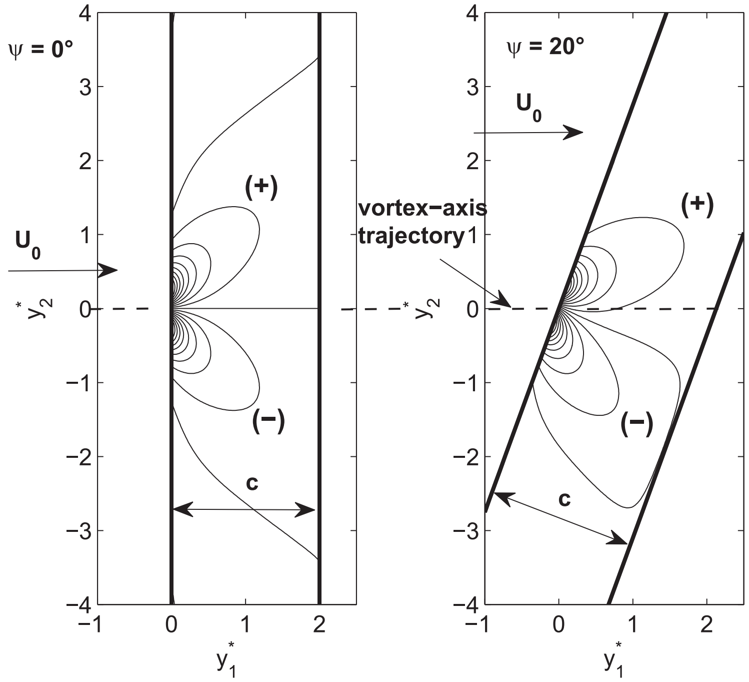

Fig. 10. Iso-contours of the regularized lift produced by all oblique gusts contributing to the impingement of the Oseen vortex at a given frequency on a rectangular airfoil, ignoring tip effects. $M_0 = 0.54$, flow from left to right, vortex axis at mid span, vortex core size $r_0 = c/8$ (same data as in Fig. 6). Positive and negative instantaneous areas indicated by $(+)$ and $(-)$, 20 iso-values between extreme values.

words supercritical responses are enhanced. But at the same time the amplitude of the induced lift is reduced by the fact that it involves the projection U_1 of the incident velocity normal to the leading edge, according to Eqs. (10) and (11). Finally no significant change of the overall amplitude of the aerodynamic response is observed in the example of Fig. 10. In view of the result introducing sweep in the analysis is believed to preserve the conclusions drawn in Section 4.3 about the effect of clipping. This will be confirmed in Section 5. Nevertheless the test of Fig. 7 could be reproduced with sweep by using the expressions of the radiation integrals for a swept parallelogram, as provided by Roger and Carazo [16].

4.5. Comments on vortex–wing interactions

Generic lift patterns induced by a helical vortex on an extended airfoil ignoring span-end effects provide a simple model of interactions occurring on various installed propellers or rotors. Typically the tip vortices shed by a pulling propeller interact with the wing of an airplane. Even though propeller noise is most often analyzed with the standpoint of equivalent sources distributed on the blades because of flow distortions induced by the installation on the aircraft, the impingement of the wakes and of the tip vortices onto the wing also generates sound, at the same multiples of the blade-passing frequency. The model expressions derived in previous sections just need being duplicated for getting a description of the propeller–wing interaction. Because the tip vortices follow helical paths originating from the blade tips their traces on the wing feature two unsteady but stationary patterns separated from each other by about a propeller diameter (or less due to stream-tube contraction) along the span of the wing, somewhat acting as two well separated quadrupoles. For an even number of blades B interacting with a zero-sweep wing both patterns have opposite phases whereas they are in phase quadrature for an odd number of blades. This rough description holds whatever the advance ratio could be. The effect of sweep is just to introduce additional phase-shift between the two induced lift patterns. At the mth multiple of the blade-passing frequency the sweep-induced phase shift is $mB\,\tan\psi/\tan\varphi$. It involves not only the sweep angle ψ but also the vortex inclination angle φ which depends on the advance ratio and blade pitch angle. Examples are given in Fig. 11. For the tested parameters with $B=8$ a sweep of 10° leads to two traces of nearly equal phases whereas the traces would be of opposite phases for zero sweep. A sweep angle of 20° again produces traces which are nearly of opposite phases. Even though the angles are given extreme values in this test, the result suggests that very different interferences can take place depending on the propeller–wing configuration. The same mechanism is expected if the wake of a CROR system impinges on a tail empennage.

The tilt-rotor and tilt-wing technologies designed for V-STOL (Vertical or Short Take-Off and Landing) applications also involve strong vortex–wing interactions. The tilt-rotor aircraft is most often made up of two powered rotors mounted on rotating shafts at the ends of short rectangular wings with zero sweep. The rotors operate in a horizontal plane for vertical take-off, somewhat like helicopter rotors. They are progressively tilted forward as the flight speed increases and behave like

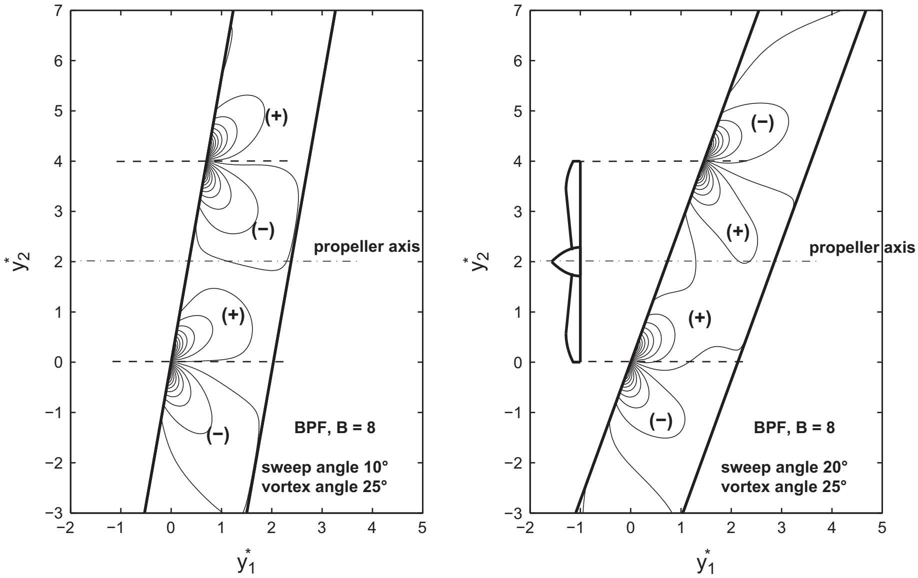

Fig. 11. Typical iso-contours of the regularized unsteady-lift distribution on a swept wing caused by tip vortices shed from a pulling propeller. Same even blade number and vortex angle at two different sweep angles. Positive and negative instantaneous areas indicated by $(+)$ and $(-)$, 20 iso-values between extreme values.

conventional pulling propellers in forward flight. The wing of tilt-rotor architectures only traverses half the meridian plane of the rotor wake, so that a single vortex impingement occurs. The tilt-wing technology is similar except that now the rotor axis and wing plane coincide. Both are tilted forward together for STOL operations. Furthermore some aircrafts such as the Hiller X-18 combine the tilt-wing architecture with counter-rotating rotors.

Acoustic assessment of the aforementioned interactions is beyond the scope of the paper. For possible further research the far-field sound associated with the lift patterns could be easily calculated from the radiation integrals of rectangles and parallelograms as derived analytically [16]. It is worth noting that a thorough investigation of propeller–wing interaction has been recently reported by Thom [2] based on unsteady RANS (Reynolds-Averaged Navier–Stokes) simulations, and compared to experimental aerodynamic results. Various aspects of the interaction were highlighted. Vortex stretching and bending around the rounded leading edge of the wing were clearly identified. The author also pointed out that the amplitude of the pressure-coefficient variations at 5 percent of chord from the leading edge, close to the location of the spots in Fig. 11, was substantially higher on the suction side than on the pressure side of the wing. This deviation from the linearized theory is a known effect of airfoil design and loading. Finally Thom post-processed the CFD data using Ffowcs Williams and Hawkings' analogy to compute the radiated sound in the vertical meridional plane of the propeller. For a typical propeller–wing distance of 1.6 tip radius, the sound radiated from the wing was found to be significant but lower by about 6 dB than the total sound radiated by the propeller, in directions normal to the wing plane. It must be stressed that according to the present derivations, wing/tip–vortex interaction does not radiate preferentially in vertical directions despite the dipolar character of the sources, but rather at sideline directions according to the lateral-quadrupole behavior suggested by the results of Section 4.2.

5. Response of a swept blade–tip

5.1. Unsteady lift correction

The tip segment of a rear-rotor blade in a CROR must be considered carefully because it is the most efficient sound generator due to its high rotational speed. It is impinged by either front-rotor tip vortices or wakes depending on the effectiveness of clipping. In any case the oncoming disturbances are split into sinusoidal gusts and the analysis relies on the aerodynamic response of the tip to an arbitrary gust. A convenient way of estimating this response is to assimilate it to the local one of an infinite flat-plate airfoil. This is done in most analytical models such as Amiet's classical theory used in preceding sections. Amiet's theory has proved its physical consistency in previously reported works, typically dealing with turbulence-impingement airfoil noise [34,35]. However a tip segment does not respond like any other segment of a blade of large span. Span-end effects are likely to modify the onset of lift fluctuations. Discarding them from the analysis is questionable for concentrated disturbances precisely impinging close to the tip. Yet the question of the tip response is seldom addressed in the literature, apart from Peake's theory of the scattering by a quarter-plane [36] ignoring the effect of the trailing edge. This context motivated the derivation of an airfoil model response explicitly accounting for the effects of span end and finite chord length. In essence the work is aimed at extending Amiet's approach without changing its mathematical background. However strong simplifications are needed to ensure tractable derivations. The mean loading of the blade tip is assumed zero, so that the impingement of incident disturbances may be addressed ignoring the formation of a tip vortex on the impinged blade. The work was started by the authors in previous papers [16,19] in the case of a rectangular, unswept blade. The interest was found in deriving a mathematically exact blade–tip response function by means of a two-directional Schwarzschild's technique. The same problem is readdressed in this section with arbitrary sweep angle of the blade tip segment, for application to the modeling of tip–vortex impingement.

The swept segment of interest is the one shown in Fig. 1b for a blade–tip section along the line $y_2^*=0$. It has a constant chord c as defined normal to the leading edge and is inclined with the sweep angle ψ. In a first step the blade segment is assumed of infinite span, y_2^* and $y_2^{'*}$ ranging from $-\infty$ to ∞ when evaluating the induced lift fluctuations, according to standard application of unsteady aerodynamic theories [27,29,16]. But actually a non-zero lift on the subspace $y_2^*>0$ does not make any sense. Therefore the lift is forced to zero beyond the tip section ($y_2^*=0$) in a second step, by adding a correction that is solution of a complementary Schwarzschild's problem in the y_2^* direction.

The correction is detailed first for the dominant leading-edge impingement term ignoring the trailing edge, and for a supercritical gust. The same would hold for sub-critical gusts again changing κ in $\mathrm{i}\kappa'$. The procedure is equivalent to consider a rigid plate over the region $y_1^{'*}>0$. In these conditions, once expressed in the system (y_1^*,y_2^*) the unsteady lift induced by a gust of wavenumbers $(k_1^{'*},k_2^{'*})$ reads

$$\tilde{\ell}_1(y_1^*,y_2^*)=\frac{A\mathrm{e}^{\mathrm{i}a_1y_1^*}\mathrm{e}^{\mathrm{i}a_2y_2^*}}{\sqrt{\cos\psi y_1^*-\sin\psi y_2^*}}\quad\text{with}\quad A=\frac{-2\rho_0U_1w_0\mathrm{e}^{\mathrm{i}\pi/4}}{\sqrt{\pi(k_1^{'*}+\beta_1^2\kappa)}},$$

$$a_1=\sin\psi\,k_2^{'*}-[\mu M_1-\kappa]\cos\psi,\quad a_2=\cos\psi\,k_2^{'*}+[\mu M_1-\kappa]\sin\psi,$$

omitting the factor $\mathrm{e}^{-\mathrm{i}\omega t}$. Recall that this expression is the trace of a pressure field solution of the convected Helmholtz equation (7). It holds uniformly for a spanwise coordinate ranging from $-\infty$ to ∞. Therefore a correction $\tilde{\ell}_2$ is introduced so that the total quantity $\tilde{\ell}=\tilde{\ell}_1+\tilde{\ell}_2$ is exactly zero for $y_2^*=0$. For physical consistency, the derivative $\partial\tilde{\ell}_2/\partial y_3^*$ must be zero on the segment surface. The correction and the total $\tilde{\ell}$ are again solutions of Eq. (7).

Schwarzschild's theorem only handles half-plane problems. In order to derive the tip correction using this theorem, the expression of the unsteady lift must be written as a function of y_2^* multiplied by sinusoidal functions of the streamwise coordinate y_1^* that can be factorized. Therefore a Fourier splitting is performed on $\tilde{\ell}_1$ considered as a function of y_1^* continued by zero upstream of the leading edge, and parametrized by the coordinate y_2^*. The Fourier transform reads

$$\hat{\ell}_1(y_2^*,\xi)=\frac{A\mathrm{e}^{\mathrm{i}a_2y_2^*}}{2\pi\sqrt{\cos\psi}}\int_{\tan\psi\,y_2^*}^{\infty}\frac{\mathrm{e}^{\mathrm{i}(a_1-\xi)y_1^*}}{\sqrt{y_1^*-\tan\psi\,y_2^*}}\,\mathrm{d}y_1^*=\frac{A(1+\mathrm{i})\mathrm{e}^{\mathrm{i}by_2^*}}{2\sqrt{\cos\psi}\sqrt{2\pi(a_1-\xi)}}$$

with $b=a_2+(a_1-\xi)\tan\psi$.

The correction $\hat{\ell}_2$ for any single wavenumber ξ is solution of the Helmholtz equation in the variables (y_2^*,y_3^*)

$$\frac{\partial^2\hat{\ell}_2}{\partial y_2^{*2}}+\frac{\partial^2\hat{\ell}_2}{\partial y_3^{*2}}+\nu^2\hat{\ell}_2=0 \tag{17}$$

with $\nu^2=(k^*-M_0\xi)^2-\xi^2$. Its normal derivative is zero in particular on the blade surface $(y_1^{'*}>0,y_2^*<0)$ and the total pressure jump $\hat{\ell}_1+\hat{\ell}_2$ is exactly zero for $y_2^*>0$. This leads to a canonical problem solved by Schwarzschild's technique, with boundary conditions

$$\hat{\ell}_2=-\hat{\ell}_1,\quad y_2^*>0,\quad \left.\frac{\partial\hat{\ell}_2}{\partial y_3^*}\right|_{y_3^*=0}=0,\quad y_2^*\le 0.$$

The associated Schwarzschild's theorem yields

$$\hat{\ell}_2(y_2^*,\xi)=-\frac{1}{\pi}\frac{A(1+\mathrm{i})}{2\sqrt{\cos\psi}\sqrt{2\pi(a_1-\xi)}}\int_0^{\infty}\sqrt{\frac{-y_2^*}{t}}\frac{\mathrm{e}^{\mathrm{i}\nu(t-y_2^*)}}{t-y_2^*}\mathrm{e}^{\mathrm{i}b^*t}\,\mathrm{d}t=-A\frac{(1+\mathrm{i})}{2\sqrt{\cos\psi}}\frac{\mathrm{e}^{\mathrm{i}by_2^*}}{\sqrt{2\pi(a_1-\xi)}}\left[1-\Phi^{(0)}\left([\mathrm{i}(\nu+b)y_2^*]^{1/2}\right)\right]$$

for negative values of y_2^*. $\Phi^{(0)}$ is the complex error function with complex arguments. Applying the inverse Fourier transform to the result yields the complete tip correction $\tilde{\ell}_2$ for $(y_1^{'*}>0,y_2^*<0)$ as

$$\tilde{\ell}_2(y_1^*,y_2^*)=-A\frac{(1+\mathrm{i})}{2\sqrt{\cos\psi}}\mathrm{e}^{\mathrm{i}a_1y_1^*}\mathrm{e}^{\mathrm{i}a_2y_2^*}\times\int_{-\infty}^{\infty}\frac{\mathrm{e}^{-\mathrm{i}(a_1-\xi)[y_1^*-\tan\psi\,y_2^*]}}{\sqrt{2\pi(a_1-\xi)}}\left[1-\Phi^{(0)}\left([\mathrm{i}(\nu+b)y_2^*]^{1/2}\right)\right]\mathrm{d}\xi. \tag{18}$$

From the asymptotic behavior of the complex error function $\Phi^{(0)}$ [22], it is easily verified that this expression exactly cancels the first-order lift $\tilde{\ell}_1$ at the tip ($y_2^*=0$) and goes to zero at large distances from the tip, as expected. The integral cannot be calculated analytically. The numerical implementation must take care of the non-unique determinations of the square root and of the function $\nu(\xi)$. If considered as a function of a complex variable, the integrand is found to have two branch cuts for large negative and positive values along the real axis. Therefore ξ is given an arbitrary small imaginary part so that the integration path remains just above the real axis for positive values of ξ and just below for negative values.

Similar derivations are made for the Kutta correction that forces the unsteady lift to zero at the trailing-edge. Once expressed in the (y_1^*, y_2^*) coordinates, the solution ignoring the tip reads

$$\tilde{\ell}_1^{TE}(y_1^*, y_2^*) = -\frac{A}{\sqrt{2}}\, e^{2ia_1/\cos\psi} e^{ia_2 y_2^*} e^{ia_1 z}\left[1-(1+i)E^*\left(2\kappa\cos\psi\,(z-\tan\psi\, y_2^*)\right)\right]$$

for $z = y_1^* - 2/\cos\psi < 0$. After a change of variable and integration by parts, the Fourier transform is obtained as

$$\hat{\ell}_1^{TE}(y_2^*, \xi) = -\frac{iA}{2\pi\sqrt{2}}\,\frac{e^{2ia_1/\cos\psi} e^{iby_1^*}}{a_1-\xi}\left\{1-\sqrt{\frac{2\kappa\cos\psi}{2\kappa\cos\psi+\xi-a_1}}\right\}.$$

Next by plugging the result in Schwarzschild's integral to get the correction at the wavenumber ξ and performing the inverse Fourier transform, the tip correction is derived as

$$\tilde{\ell}_2^{TE}(y_1^*, y_2^*) = \frac{iAe^{ia_1 y_1^*} e^{ia_2 y_2^*}}{2\pi\sqrt{2}} \int_{-\infty}^{\infty} \frac{e^{2i(a_1-\xi)/\cos\psi}}{a_1-\xi}\left\{1-\sqrt{\frac{2\kappa\cos\psi}{2\kappa\cos\psi-(a_1-\xi)}}\right\} \times e^{-i(a_1-\xi)[y_1^*-\tan\psi\, y_2^*]}\left[1-\Phi^{(0)}\left([i(\nu+b)y_2^*]^{1/2}\right)\right] d\xi \tag{19}$$

where the integral is taken in Cauchy's principal value sense.

Eqs. (18) and (19) reduce to the ones given by Roger and Carazo [16] as the sweep angle ψ is set to zero. The complete procedure provides the distributed unsteady lift for any incident oblique gust, with the classical inverse-square root singularity at the leading edge and zero lift both along the trailing edge and along the tip section $y_2 = 0$. The far-field sound is obtained by a radiation integral to be computed by standard numerical quadrature. For the present tip–vortex interaction noise modeling, computations are repeated for the extended range of spanwise wavenumbers required to synthesize the incident vortex.

The effect of the tip correction on the unsteady lift response of a swept blade tip to incident isolated gusts is illustrated in Fig. 12, in both cases of supercritical and sub-critical gusts. The reference solution identical to Adamczyk's formulas is presented on the left-hand side, and the corrected solution according to Eqs. (18) and (19) on the right-hand side.

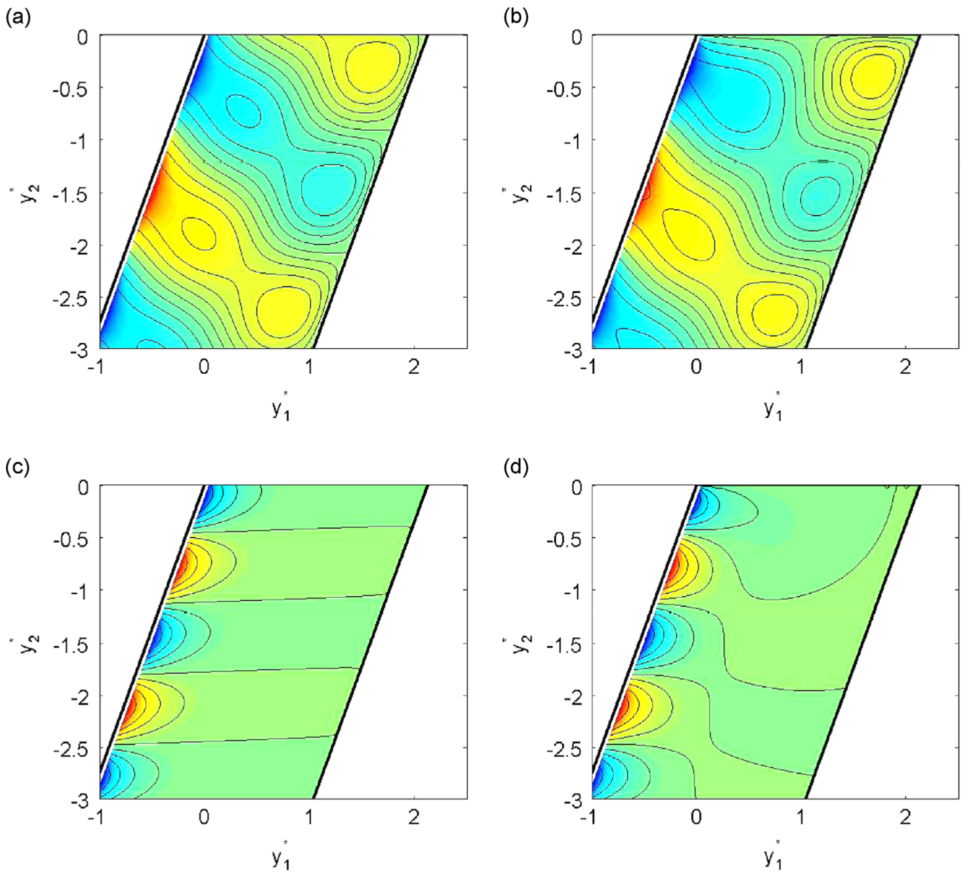

Fig. 12. Instantaneous colormaps of the unsteady lift induced on the tip of a swept airfoil by an oblique gust, without (a, c) or with (b, d) tip correction. Sweep angle $\psi = 20^\circ$, $M_0 = 0.5$. Singular leading-edge vicinity removed. Top (a, b): supercritical gust ($\mu = 4.1882, k_2^*/(\beta\mu) = 0.6838$). Bottom (c, d): sub-critical gust ($\mu = 3.7798, k_2^*/(\beta\mu) = 1.3156$). Iso-contours of the regularized lift are superimposed, with ten iso-values between extreme values. Arbitrary scales. (For interpretation of the references to color in this figure caption, the reader is referred to the web version of this article.)

The colormaps illustrate instantaneous lift distributions. The very leading-edge vicinity is not shown in order to avoid saturation of the map caused by the inverse square-root singularity. This is why as in previous figures iso-contours of the regularized lift are superimposed as black lines to emphasize the left–right differences. Oblique wavefronts are clearly identified for the supercritical gust whereas the evanescent behavior of the sub-critical gust results in a more concentrated trace at the leading edge. The unsteady lift is forced to zero along the tip section by the proposed correction, and the associated modifications affect the airfoil surface with some attenuation away from the tip. It must be noted that residual inaccuracies hardly visible on the plots are produced at the very trailing edge, with no noticeable effect on subsequent acoustic calculations.

Typical unsteady lift patterns resulting from the impingement of the Oseen vortex are next reported in Fig. 13. Three positions of the vortex-core path relative to the blade tip are considered, for inward impingement, impingement exactly at the tip and a vortex passing beyond the tip. For this test the origin of coordinates is kept on the tip section of the blade and the vortex axis is displaced along y_2. The corresponding values of e/r_0 are -3.2, 0 and 3.2, respectively. The instantaneous plus and minus half-spots are identified as the white and black parts of the traces. In the case $e/r_0 = 3.2$ only a part of the negative half-spot impinges on the segment surface. Because the tip correction forces the response to zero along the tip section the amplitude of the half-spot is substantially reduced. The expected reduced sound radiation will be confirmed in the next section. The effect of the correction is minor in the case $e/r_0 = 0$ because the unsteady lift is already close to zero along the tip section without the correction by virtue of the anti-symmetry of the complete trace. Similarly the effect of the correction in the case $e/r_0 = -3.2$ is significant but not strong.

It is worth noting that in the present formulation the tip is parallel to the oncoming flow, along $y_2 = 0$. The solving procedure forces the pressure jump to zero at the tip and beyond; this makes the tip interpreted as a trailing edge. Equivalent results would be obtained using the velocity potential instead of the pressure jump in this case, because the relationship between pressure and potential only involves a derivative with respect to y_1. The same pressure-based formulation would hold as well for an oblique tip of equation $y_2 = \chi y_1$ with $\chi < 0$; indeed the tip would be a true inclined trailing edge. In contrast a tip of equation $y_2 = \chi y_1$ with $\chi > 0$ would be equivalent to a swept leading edge. A zero velocity potential should now be imposed beyond the tip, which makes a strong difference due to the aforementioned derivative. Though this was not attempted in the study, it is guessed that a totally different result would be derived, with the characteristic inverse-square root singularity instead of the pressure release along the tip.

5.2. Far-field radiation

The far-field sound radiation for a swept blade tip is addressed in this section by generalizing the radiation integrals of Section 4.2. Referring to the stretched coordinate systems introduced in Fig. 1b and attached to the parallelogram airfoil, the radiation integral can be written as

$$\tilde{p}(\mathbf{x},\omega) = \frac{\mathrm{i}k^* x_3 c}{8\pi S_0^2} \cos\psi \int_{-2L/(c\cos\psi)}^{0} \int_{0}^{2/\cos\psi} \tilde{\ell}\,(y_1^*, y_2'^*)\, \mathrm{e}^{\mathrm{i}k^*(M_2-\beta_1^2 x_2/S_0) y_2'^*/\beta^2} \times \mathrm{e}^{\mathrm{i}k^*[(M_1-\beta_2^2 x_1/S_0)\cos\psi + (M_2-\beta_1^2 x_2/S_0)\sin\psi] y_1^*/\beta^2}\, \mathrm{d}y_1^*\, \mathrm{d}y_2'^*. \tag{20}$$

The origin is defined at the leading-edge corner of the swept blade tip. It is worth noting that with respect to the underlying geometric far-field assumption, it could be equivalently chosen at the segment center point. The integral must be solved numerically because the resulting lift distribution has no closed-form expression and, in particular, cannot be factorized as separate functions of y_1^* and $y_2'^*$. The three-dimensional directivity diagrams corresponding to the three configurations of Fig. 13 and to the additional one $e/r_0 = 8$ are reported in Fig. 14. The directivity lobes computed ignoring the tip correction are plotted as the black mesh and the ones computed with the correction included as the gray faceted surfaces. The direction of the incident flow and the trajectory of the vortex-core axis are indicated in the plots, and different view angles are selected for the sake of clarity. Axis units are arbitrary but the same for all plots. The segment surface is featured by the gray parallelogram. For inward impingement close to the tip (upper left plot, $e/r_0 = -3.2$), the uncorrected calculations predict oblique lobes that are similar to the quadrupole-like patterns illustrated in Section 4.2, except that the two lobes pointing outward are of smaller amplitude (hidden in the figure). The correction has the effect of reducing the main oblique lobes and of producing less focused, distorted dipole-like lobes. Despite the very different radiation patterns, the total acoustic power remains the same, as confirmed below. Impingement exactly at the tip (upper right plot, $e/r_0 = 0$) generates very similar patterns with or without the tip correction. The lobes are just slightly distorted. The passage of the vortex closely beyond the tip (lower left plot, $e/r_0 = 3.2$) tends to radiate with two oblique lobes pointing inwards. The effect of the correction is to significantly reduce the sound amplitude with only a small angular shift of the lobes. The reduction is expected from the lift distribution of Fig. 13(bottom). Finally for a vortex core passing well beyond the tip (lower right plot, $e/r_0 = 8$), the sound radiation drops dramatically for both the uncorrected and corrected calculations. Surprisingly the radiation is enhanced with the corrected calculations, but the sound remains weak with only a power increase of 1 dB. This is attributed to a more favorable conjunction of the phase distribution of the sources when the correction is applied.

For a better overall estimate of the acoustic efficiency, the radiated power is again reported in Fig. 15 as a function of e/r_0, in the same way as in Section 4.2, for the first three configurations. The results with the Oseen vortex already presented in

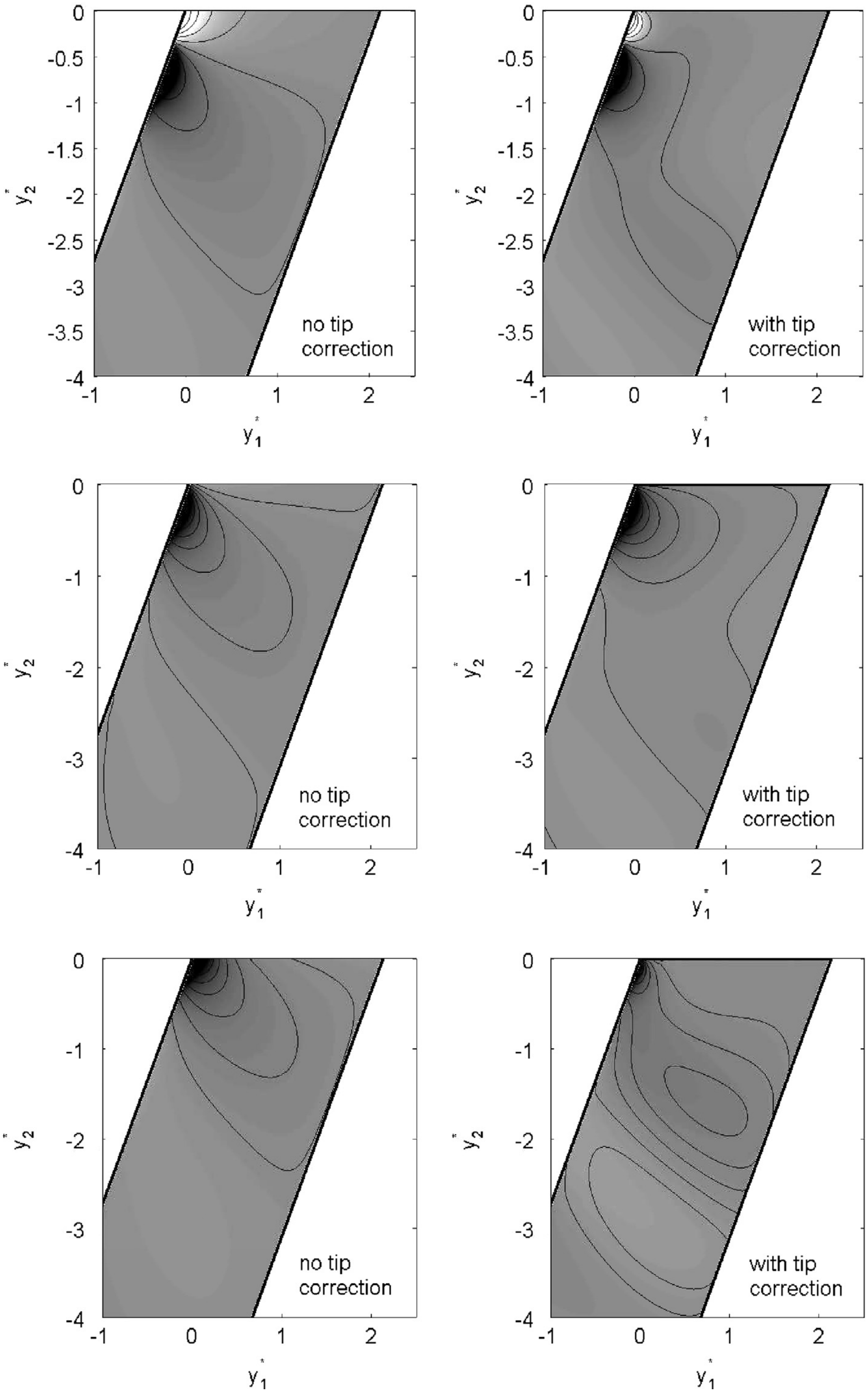

Fig. 13. Instantaneous maps of the unsteady lift induced on the tip of a swept airfoil by the Oseen vortex, without (left) or with (right) tip correction. Singular leading-edge vicinity removed. Impingement inward (top, $e/r_0 = -3.2$), at tip (middle, $e/r_0 = 0$) and beyond the tip (bottom, $e/r_0 = +3.2$). Superimposed iso-contours of the regularized lift with ten iso-values between extreme values. Arbitrary scales. $M_0 = 0.54$, $\mu = 2.7$, $\psi = 20°$, flow from left to right, vortex core size $r_0 = c/8$ (same data as in Fig. 6).

Fig. 7 for the unswept blade tip and without correction are reproduced, and a vertical shift is applied to make relative variations comparable. The new calculations are emphasized by the rectangular boxes. Globally the effect of the interaction distance is the same for unswept and swept blade tips, and whether the tip correction is applied or not.

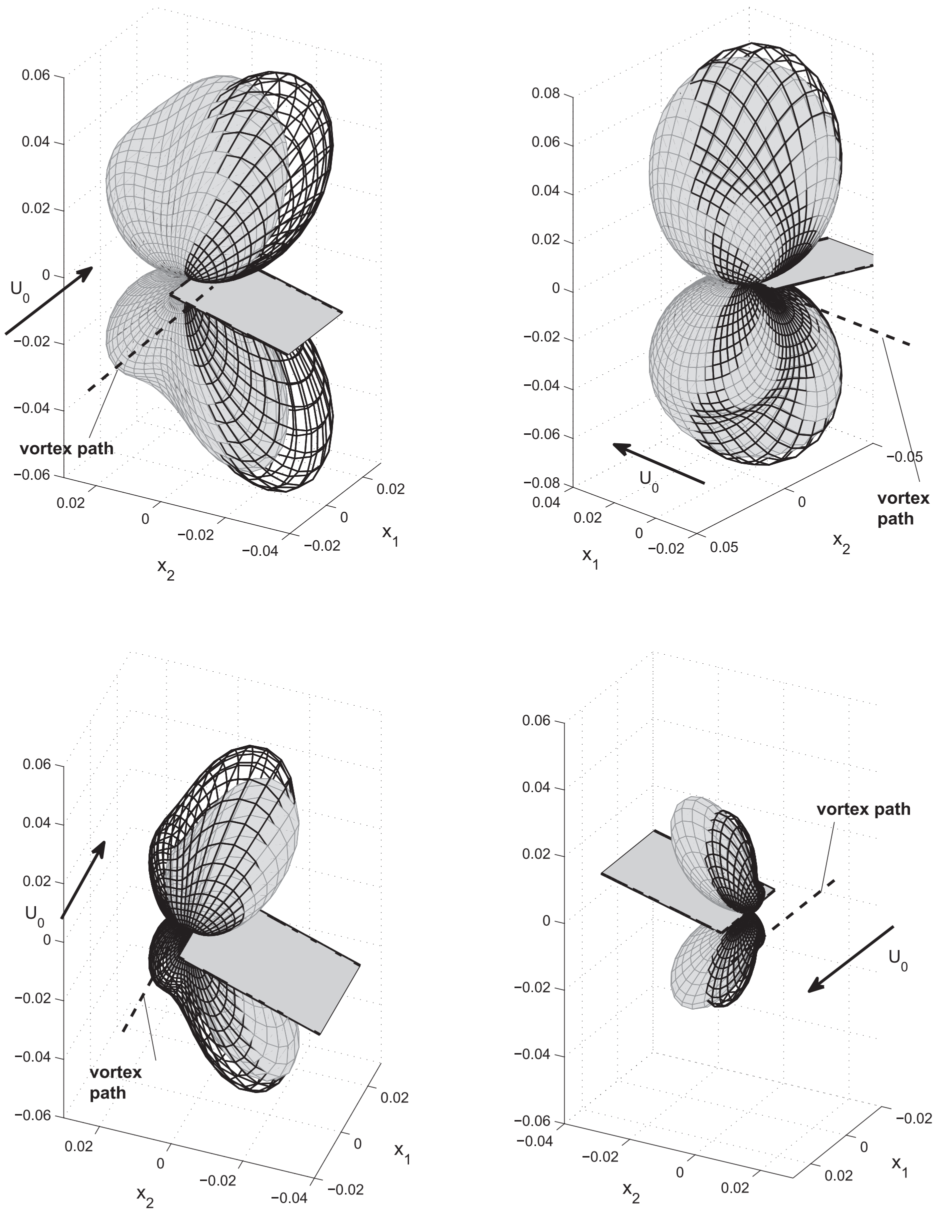

Fig. 14. Directivity diagrams of blade–tip vortex interaction noise in various configurations. Sweep angle 20°. Ignoring (black meshes) or accounting for (gray surfaces) tip-response correction. From upper left to lower right, values of e/r_0: -3.2, 0, 3.2, 8. Arbitrary scale, identical on all plots.

In particular impingement at tip is the loudest configuration. However in the special case $e/r_0 = 3.2$ the predictions with the correction are 2 dB below the uncorrected ones, in accordance with the corresponding plots of Figs. 13 and 14. Finally, both sweep and tip corrections have a significant effect on the radiated sound field but this effect typically remains in the order of a couple of decibels on the integrated power.

6. Conclusions

A three-step analytical model for assessing fundamental aspects of blade–tip/tip–vortex interaction noise in counter-rotating open rotors has been developed. The first step is the description of the vortices shed by the blades of the front rotor and their expansion in a set of oblique gusts with respect to a reference frame attached to the impinged rear-rotor blade segment. The very details of the spinning-velocity distribution of the vortex have been found to have a minor effect on the results, as far as the vortex-core radius and the maximum velocity are the same. This is because the main differences are in the outer part of the vortex and are canceled as multiple vortices are arranged periodically. Therefore the Oseen vortex has

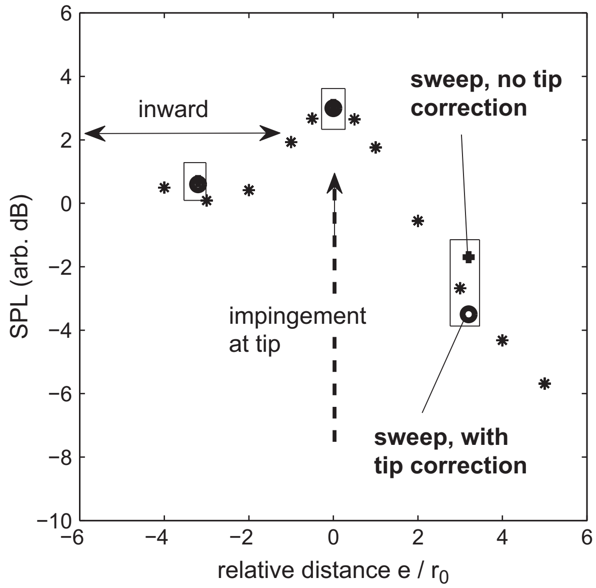

Fig. 15. Effect of relative vortex-to-tip distance on the radiated acoustic power. New calculations for a swept blade featured by the small boxes, ignoring or accounting for tip-response correction. Oseen vortex, same configurations as in Fig. 13. Vortex core size $r_0 = c/8$. Arbitrary dB scale. Thin symbols $*$ dealing with a zero-sweep blade reproduced from Fig. 7 for comparison.

been selected as a relevant model for the whole study. The second step is the derivation of the induced unsteady lift on the blade segment accounting for sweep, for both isolated gusts and for the complete trace of the vortex. The last part is the derivation of a tip correction for the aerodynamic response of the blade segment. Preliminary results and a first analysis have been given about the effect of the main parameters on the blade loading, as well as on the radiated noise in the reference frame of the segment.

The unsteady lift induced by a tip vortex on a spanwise-extended surface is characterized by a concentrated pattern made up of a pair of upwash and downwash dipoles. The latter tend to cancel each other and behave like an equivalent lateral quadrupole. The first and dominant effect of the blade termination is the truncation of the lift pattern that would be induced on an airfoil of infinite span, resulting in modified interferences in the sound field. Oblique dipole-like radiation lobes are produced if the blade tip escapes part of the trace of the vortex, because the upwash/downwash cancellation is less effective. Based on the truncation as the only involved mechanism and on the assumption of an unswept rectangular blade tip, the maximum sound production is observed as the vortex-path radius coincides with the tip radius of the blade. Inward vortex impingement is less efficient because of the aforementioned quadrupole behavior. A vortex passage farther away beyond the tip is beneficial, with an acoustic power decrease with a distance of about 2 dB per core radius of the vortex. Sweep and tip correction lead to the same overall conclusions, despite the modifications they introduce in the unsteady lift patterns. More fundamentally, vortex impingement can only be described by considering both supercritical and sub-critical gusts in the usual sense of unsteady aerodynamics.

The effect of the span end on the aerodynamic response has been derived by resorting to an original application of Schwarzschild's technique in the radial direction, at the price of additional space Fourier transforms in the streamwise direction. The corrected lift is expressed as an integral that requires numerical quadrature for the implementation of the model. The advantage of the solution is that the same mathematical background is used as for the classical derivation of the unsteady lift on an airfoil of infinite span. When the tip correction is introduced in the modeling, the induced lift is set to zero at the tip of the blade segment in the same way as what is imposed by the Kutta condition at the trailing-edge. This reduces the amplitude of the equivalent acoustic sources and redefines their relative phases. The proposed correction only holds for a tip section aligned with the relative flow direction. The mathematical problem should be re-addressed in other configurations.

Even though the total radiated power and its variation with the vortex distance to the tip appear as weakly sensitive to both sweep and tip correction by virtue of the averaging over all directions, the directivity diagrams differ more significantly. The iso-contours of the unsteady lift are modified by the tip correction and by the inclination of the leading and trailing edges, with respect to the classical response of a rectangular unswept blade. This redistributes the phase and amplitude of the acoustic sources in such a way that the resulting sound is hardly previsible. Up to that point the present results stress that sweep and span-end effects should be accounted for in any prediction model of CROR interaction noise, especially when dealing with vortex-impingement noise, if the targeted accuracy is within the couple of decibels. In this way the acoustic benefit of clipping the rear rotor can be assessed quite simply resorting to the present analytical developments and their implementation in optimization algorithms. When applied to propeller tip–vortex impingement on the wing of an airplane, the methodology indicates that quadrupole-like lift patterns are produced at each impinging point of the vortices. The model expressions derived in the paper could be used for a rough estimate of the associated noise. That noise preferentially radiates sideline.

References

[1] A.R. George, S.T. Chou, *Helicopter Tail Rotor Blade–Vortex Interaction Noise*, NASA CR-183178, 1986.
[2] A.D. Thom, Analysis of Vortex-Lifting Surface Interactions, PhD Thesis, University of Glasgow, College of Science & Engineering, 2011.
[3] J.E. Ffowcs Williams, D.L. Hawkings, Sound generation by turbulence and surfaces in arbitrary motion, *Philosophical Transactions of the Royal Society A* 264 (1969) 321–342.
[4] M.E. Goldstein, *Aeroacoustics*, McGraw-Hill, NY, 1976.
[5] A. Stuermer, J. Yin, Aerodynamic and aeroacoustic analysis of contra-rotating open rotor propulsion systems at low-speed flight conditions. in: A. Dillmann, G. Heller, M. Klaas, H.P. Kreplin, W. Nitsche, W. Schröder (Eds.), *New Results in Numerical and Experimental Fluid Mechanics VII, Notes on Numerical Fluid Mechanics and Multidisciplinary Design (NNFM)*, vol. 112, Springer Verlag, 2010.
[6] F. Falissard, R. Boisard, G. Delattre, Aeroacoustic computation of a contra-rotating open rotor model with test rig installation effects, *18th AIAA/CEAS Aeroacoustics Conference*, Paper 2012–2218, Colorado Springs CO, 2012.
[7] Y. Colin, A. Carazo, B. Caruelle, T. Node-Langlois, A.B. Parry, Computational strategy for predicting CROR noise at low speed. Part 1. Review of the numerical methods, *18th AIAA/CEAS Aeroacoustics Conference*, Paper 2012–2221, Colorado Springs CO, 2012.
[8] L. Soulat, I. Kernemp, M. Sanjose, S. Moreau, R. Fernando, Assessment and comparison of tonal noise models for counter-rotating open rotors, *19th AIAA/CEAS Aeroacoustics Conference*, Paper 2013–2201, Berlin, Germany, 2013.
[9] V.P. Blandeau, P.F. Joseph, Broadband noise due to rotor–wake/rotor interaction in contra-rotating open rotors, *AIAA Journal* 48 (11) (2010) 2674–2686.
[10] M.S. Howe, Contributions to the theory of sound production by vortex–airfoil interaction, with application to vortices with finite axial velocity defect, *Proceedings of the Royal Society of London* A-420 (1988) 157–182.
[11] R.K. Amiet, Airfoil gust response and the sound produced by airfoil–vortex interaction, *Journal of Sound and Vibration* 107 (3) (1986) 487–506.
[12] J.S. Marshall, Vortex cutting by a blade. Part I. General theory and a simple solution, *AIAA Journal* 32 (6) (1994) 1145–1150.
[13] J.S. Marshall, R. Yalamanchili, Vortex cutting by a blade. Part II. Computations of vortex response, *AIAA Journal* 32 (7) (1994) 1428–1436.
[14] F. Obermeier, K.Q. Zhu, Sound generation by rotor–vortex interaction in low Mach number flow, *Journal of Aircraft* 30 (1) (1993) 81–87.
[15] F.G. Leppington, R.A. Sisson, On the interaction of a moving hollow vortex with an aerofoil, with application to sound generation, *Journal of Fluid Mechanics* 345 (1997) 203–226.
[16] M. Roger, A. Carazo, Blade-geometry considerations in analytical gust–airfoil interaction noise models, *16th AIAA/CEAS Aeroacoustics Conference*, Paper 2010–3799, Stockholm, Sweden, 2010.
[17] A. Carazo, M. Roger, M. Omais, Analytical prediction of wake–interaction noise in counter-rotating open rotors, *17th AIAA/CEAS Aeroacoustics Conference*, Paper 2011–2758, Portland, OR, 2011.
[18] M.J. Kingan, R.H. Self, Counter-rotation propeller tip vortex interaction noise, *15th AIAA/CEAS Aeroacoustics Conference*, Paper 2009–3135, Miami, FL, 2009.
[19] M. Roger, C. Schram, Analytical modelling of the tonal noise from open rotors due to tip vortices, *ISROMAC-14*, Honolulu, HI, 2012.
[20] M. Roger, C. Schram, S. Moreau, On open rotor blade–vortex interaction noise, *18th AIAA/CEAS Aeroacoustics Conference*, Paper 2012–2216, Colorado, Springs CO, 2012.
[21] I.S. Gradshteyn, I.M. Ryzhik, *Tables of Integrals, Series and Products*, 6th edition, Academic Press, NY, 2000.
[22] M. Abramowitz, I.A. Stegun, *Handbook of Mathematical Functions*, Dover, NY, 1965.
[23] L. Soulat, I. Kernemp, S. Moreau, R. Fernando, Numerical assessment of the noise emission of counter-rotating open rotors, *10th European Turbomachinery Conference*, Paper 210, Lappeenranta, 2013.
[24] D.B. Hanson, D.J. Parzych, *Theory for Noise of Propellers in Angular Inflow With Parametric Studies and Experimental Verification*, NASA CR 4499, 1993.
[25] J.M.R. Graham, Similarity rules for thin aerofoils in non-stationary subsonic flows, *Journal of Fluid Mechanics* 43 (4) (1970) 753–766.
[26] M. Landahl, *Unsteady Transonic Flow*, Pergamon Press, NY, 1961.
[27] R.K. Amiet, High frequency thin-airfoil theory for subsonic flow, *AIAA Journal* 14 (8) (1976) 1076–1082.
[28] R.K. Amiet, Acoustic radiation from an airfoil in a turbulent stream, *Journal of Sound and Vibration* 41 (4) (1975) 407–420.
[29] J.J. Adamczyk, *The Passage of an Infinite Swept Airfoil through an Oblique Gust*, NASA CR 2395, 1974.
[30] P.F. Mish, W.J. Devenport, An experimental investigation of unsteady surface pressure on an airfoil in turbulence. Part 1. Effects of mean loading, *Journal of Sound and Vibration* 296 (3) (2006) 417–446.
[31] S. Moreau, M. Roger, V. Jurdic, Effect of angle of attack and airfoil shape on turbulence-interaction noise, *11th AIAA/CEAS Aeroacoustics Conference*, Paper 2005–2973, Monterey, CA, 2005.
[32] M. Roger, On broadband jet–ring interaction noise and aerofoil turbulence-interaction noise predictions, *Journal of Fluid Mechanics* 653 (2010) 337–364.
[33] A.R. Ahmadi, *An Experimental Investigation of the Chopping of Helicopter Main Rotor Tip Vortices by the Tail Rotor*, NASA CR-177338, 1984.
[34] R.W. Paterson, R.K. Amiet, *Acoustic Radiation and Surface Pressure Characteristics of an Airfoil due to Incident Turbulence*, NASA CR-2733, 1976.
[35] M. Roger, S. Moreau, Extensions and limitations of analytical airfoil broadband noise models, *International Journal of Aeroacoustics* 9 (3) (2010) 273–305.
[36] N. Peake, Unsteady transonic flow past a quarter-plane, *Journal of Fluid Mechanics* 244 (1992) 377–404.